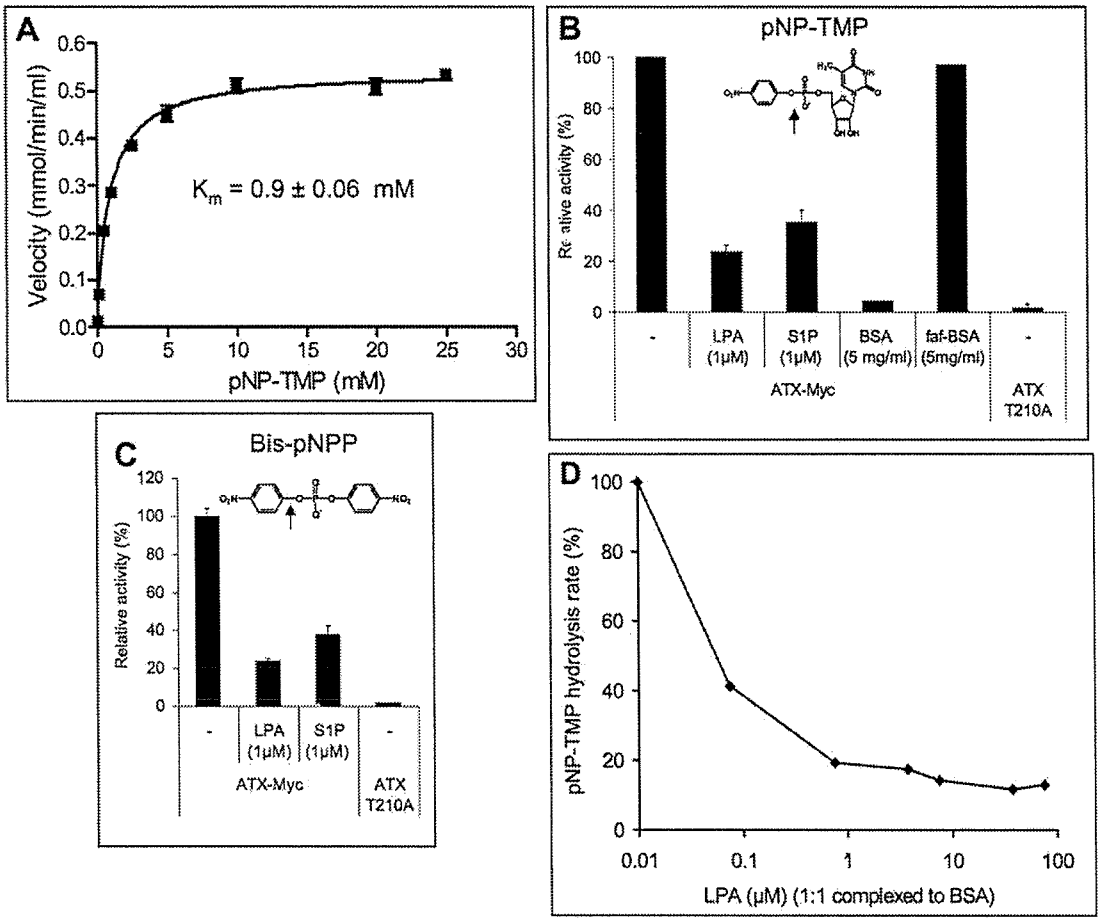

FIG. 3. **ATX-catalyzed hydrolysis of non-lipid substrates.** *A*, hydrolysis of pNP-TMP. Initial rates of pNP formation, measured over 3 h by light absorbance, are plotted against increasing substrate concentrations and fitted according to the Michaelis-Menten equation using GraphPad software. *B*, hydrolysis of pNP-TMP (1 mM). LPA (1-oleoyl) and S1P were added at 1 μM. BSA and delipidated BSA (*faf-BSA*; 99% fatty acid-free) were added at 5 mg/ml. *ATX T210A* represents catalytically inactive ATX. *Inset*, structure of pNP-TMP; *arrow* indicates the phosphodiesterase cleavage site. *C*, hydrolysis of bis-pNPP (1 mM). LPA and S1P were added at 1 μM. *Inset*, structure of bis-pNPP; *arrow* indicates the phosphodiesterase cleavage site. *D*, inhibition of pNP-TMP hydrolysis by increasing concentrations of 1-oleoyl-LPA, complexed to delipidated BSA (1:1 molar ratio). pNP-TMP was used at 1 mM.

of the cleavable signal sequence from influenza hemagglutinin, and cloned into a mammalian expression vector driven by the SR-α promoter. After linearization, the DNA was transfected into Chinese hamster ovary cells, and a highly expressing stable transfectant was isolated by single cell cloning. The soluble enzyme was purified from culture supernatants by sequential chromatography consisting of large scale anion exchange chromatography, Blue-Sepharose, AMP-Sepharose, and final polishing on a Uno-Q column (Bio-Rad). Purity was confirmed by SDS-PAGE and silver staining.

lyso-PLD Assay—To measure lyso-PLD activity, radiolabeled LPC (1-[1-^{14}C]palmitoyl, Amersham Biosciences) and unlabeled LPC (1 μM) were dried under nitrogen, and the mixture was reconstituted in Tris-buffered saline (140 mM NaCl, 5 mM KCl, 1 mM $CaCl_2$, 1 mM $MgCl_2$, adn 50 mM Tris, pH 8.0) and sonicated, and BSA (2 mg/ml) was added. The reaction was started by the addition of ATX-containing conditioned medium. Lipids were extracted with butan-1-ol. All of the solutions were made 0.02 M in acetic acid and extracted with 0.5 volume of butan-1-ol as described previously (22). In brief, after thorough mixing and centrifugation, the butan-1-ol phase was removed, and the water phase was extracted once again. Butanol fractions were washed with 1 volume of butan-1-ol-saturated water and dried under nitrogen. Phospholipids were separated by thin layer chromatography on silica gel-60 plates in chloroform/methanol/acetic acid/water (50:30:8:4). Lipids were detected by autoradiography.

Phosphodiesterase Assays—Phosphodiesterase activity toward pNP-TMP and bis-pNPP was measured by light absorbance. 40 μl of HEK293T-conditioned medium was added to 160 μl of Tris-buffered saline (140 mM NaCl, 5 mM KCl, 1 mM $CaCl_2$, 1 mM $MgCl_2$, and 50 mM Tris, pH 8.0) containing pNP-TMP or bis-pNPP in 96-well plates. After incubation for 3 h at 37 °C, the amount of liberated *para*-nitrophenolate (pNP) was determined by reading the absorbance at 405 nm in a Victor Wallac plate reader.

CPF4 FRET Assay—CPF4 was synthesized as described previously (26) and maintained as a 10-mM stock solution in Me_2SO. Recombinant ATX in Tris-buffered saline (140 mM NaCl, 5 mM KCl, 1 mM $CaCl_2$, 1 mM $MgCl_2$, 50 mM Tris, pH 8.0) or ATX-Myc-containing conditioned Dulbecco's modified Eagle's medium (buffered with 50 mM Tris, pH 8.0) was incubated with or without the indicated reagents, and CPF4 was added at a concentration of 2 μM unless indicated otherwise. CPF4 fluorescence was monitored (at 37 °C) in a BMG Fluorstar 96-well plate reader (excitation at 355 nm, emission at 460 and 520 nm). Curve fitting was carried out using GraphPad software.

Fluorescence Microscopy—Cells transfected with ATX-GFP or LPA_1-GFP (28) were fixed with ice-cold methanol at 24 h after transfection. ATX and LPA_1 were detected by anti-GFP antibody using a Leica confocal microscope.

RESULTS AND DISCUSSION

ATX Processing in HEK293 Cells—ATX is synthesized as a type II transmembrane glycoprotein of ~125 kDa, consisting of a very short N-terminal region, a single transmembrane domain, and a large catalytic ectodomain. ATX undergoes membrane-proximal cleavage to yield a soluble enzyme (29), yet

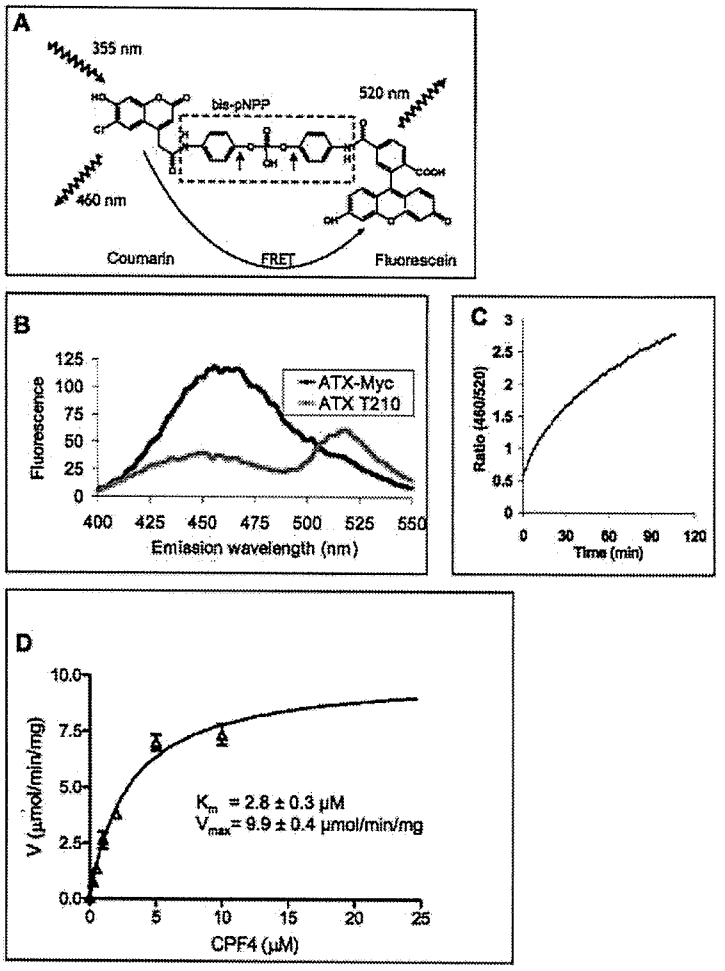

FIG. 4. **FRET-based biosensor CPF4 as an ATX substrate.** *A*, the structure of CPF4 and the mechanism of FRET (for details see Ref. 26). *B*, loss of CPF4 FRET induced by ATX-Myc, as detected by an increase in donor fluorescence and a decrease in acceptor fluorescence (*blue trace*). CPF4 concentration, 2 μM. The inactive mutant ATX(T210A)-Myc served as a negative control (*red trace*). *C*, time-dependent increase in loss of FRET induced by ATX, detected as an increase in the ratio between the fluorescence of the donor and that of the acceptor. CPF4 concentration, 2 μM. *D*, saturation kinetics of CPF4 hydrolysis by purified recombinant ATX. CPF4 hydrolysis by ATX-Myc in conditioned medium shows the same saturation kinetics (see Fig. 6).

little is known about ATX biosynthesis and proteolytic processing. In particular, it remains unclear whether the transmembrane form of ATX is expressed on the cell surface.

As a starting point for the present studies, we expressed full-length ATX in HEK293T cells using three differently HA- and Myc-tagged constructs and analyzed ATX expression in cell lysates as well as in the culture medium. As shown in Fig. 1*A*, full-length ATX is detected only in cell lysates, whereas ATX in the medium lacks the N-terminal HA tag, consistent with secreted ATX being produced by cleavage of the N terminus. The Golgi-disturbing agents brefeldin A and monensin blocked ATX secretion, indicating involvement of the classical export route (supplemental Fig. 1*A*). When analyzed by confocal microscopy, ATX is detected in intracellular vesicles but not at the plasma membrane; in contrast, LPA_1 receptors localize primarily to the cell surface under the same experimental conditions (Fig. 1*B*). From these results we conclude that ATX follows the classical secretory pathway and that proteolytic removal of its N terminus, including the transmembrane region, occurs intracellularly rather than at the plasma membrane.

ATX Activity toward Lipid and Non-lipid Substrates—Having established that ATX is not detectable as a plasma membrane-anchored ecto-enzyme, we set out to examine the catalytic activity of soluble ATX. To this end, we used conditioned medium from ATX-Myc-transfected HEK293T cells without further purification or, in some experiments, ATX purified from Sf9 cell supernatant (supplemental Fig. 1*B*). The catalytically inactive mutant ATX(T210A) served as a negative control (27).

The lyso-PLD activity of ATX was measured by the conversion of LPC(16:0) to LPA using thin layer chromatograpy (Fig. 2*A*). LPC hydrolysis by ATX proceeded at a constant rate for at least 90 min (Fig. 2*C*, *left panel*). The K_m for LPC was estimated at ~150 μM, in agreement with previously reported values (100–260 μM) (11, 12, 14) and in the range of normal LPC levels in plasma (25). When screening multiple lipids as potential modulators of lyso-PLD activity, we observed that ATX-catalyzed LPC hydrolysis was significantly inhibited by LPA and S1P (1 μM, complexed to albumin). Other phospholipids tested, including phosphatidic acid, did not show such an effect (Fig. 2 and results not shown). This suggests that ATX is subject to product inhibition by LPA. Detailed analysis of lyso-PLD inhibition is obscured, however, by limitations with the standard LPC hydrolysis assay, which generates concentrations of LPA in excess of its inhibition constant (see below). As a result, formation of LPA during the course of the assay causes the apparent inhibition of ATX by added LPA to be less pronounced than the true inhibition.

To avoid the complications of lipid product inhibition and the limitations of end-point LPC hydrolysis assays, we took advantage of the fact that ATX uses a common reaction mechanism for the hydrolysis of lipid and non-lipid substrates (20, 21). As non-lipid substrates, we tested pNP-TMP, a standard NPP substrate, and the symmetric phosphodiester bis-pNPP, a sub-

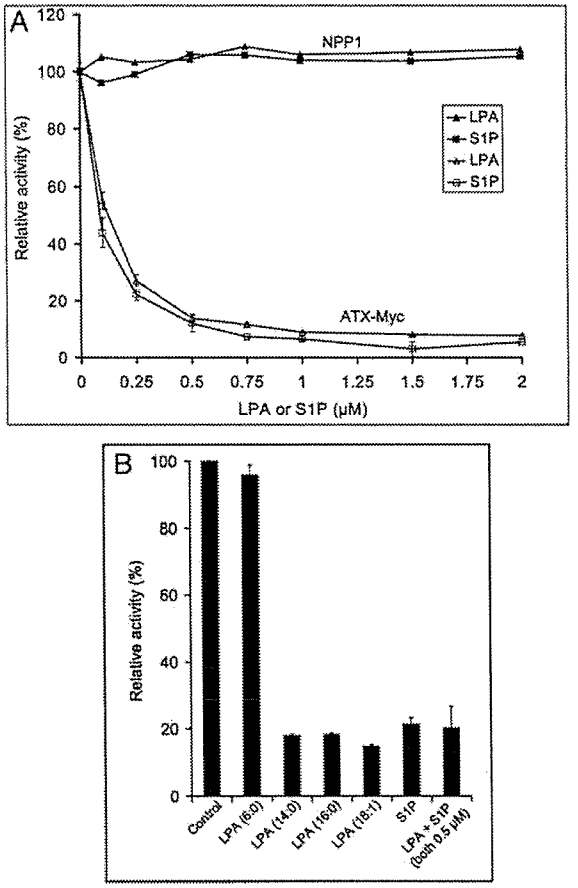

FIG. 5. **ATX inhibition by LPA and S1P.** *A*, dose-response curves for the inhibitory effects of LPA (1-oleoyl) and S1P on the activity of ATX-Myc and purified NPP1 (about 2 μg/100 μl of assay volume). CFP4 concentration, 2 μM. *B*, dependence of ATX inhibition on the acyl chain length of LPA (1 μM). The *rightmost* bar shows that the inhibitory effects of LPA and S1P (both added at 0.5 μM) are not additive.

strate for type I phosphodiesterases and certain bacterial PLDs (30–32). The liberated product, pNP, was quantified colorimetrically. As shown in Fig. 3*A*, hydrolysis of pNP-TMP followed Michaelis-Menten kinetics with a K_m of 0.9 mM, somewhat lower than the value reported by others (12). ATX was also capable of hydrolyzing bis-pNPP (Fig. 3*C*), in keeping with a previous report (21). bis-pNPP hydrolysis rates were half-maximal at ~0.5 mM but did not obey Michaelis-Menten kinetics, apparently because of substrate inhibition at higher concentrations (>1 mM; results not shown).

Similar to what is observed with LPC as a substrate, the hydrolysis of pNP-TMP and bis-pNPP by ATX was significantly inhibited by LPA and S1P (1 μM) (Fig. 3, *B* and *C*). It thus appears that, importantly, LPA and S1P exert their inhibitory effect regardless of the nature of the substrate.

Effects of BSA—Using pNP-TMP as a substrate, we observed that ATX activity was strongly inhibited by normal serum albumin (BSA) at concentrations of >50 μg/ml (0.75 μM; ~0.1% of the concentration in fetal calf serum). In marked contrast, delipidated BSA (Fig. 3*B*, *faf-BSA*) had no inhibitory effect, even when added at high concentrations (5 mg/ml; 75 μM). The observation that albumin is the major binding protein for LPA and S1P strongly suggests that ATX inhibition by "normal" BSA is largely due to these lysophospholipids. When LPA was complexed to delipidated albumin (at a 1:1 molar ratio), we found that its ability to inhibit ATX was not affected. As can be inferred from Fig. 3*D*, the IC_{50} value for the LPA·BSA (1:1) complex to inhibit ATX was close to 0.1 μM, using a substrate concentration of 1 mM (*i.e.* equal to the K_m).

CPF4, a FRET-based Sensor of ATX Activity—Because the pNP-TMP colorimetric assay showed only moderate sensitivity (detection limit, ~0.15 μg of ATX/ml), we explored a newly developed FRET-based phosphodiesterase sensor termed CPF4 (26). CPF4 is a bis-pNPP-derived probe, in which both phenyl moieties are linked to coumarin and fluorescein, respectively, resulting in FRET with high efficiency (Fig. 4*A*). Cleavage of the phosphodiester group by a nonspecific phosphodiesterase from snake venom causes loss of FRET, providing a convenient ratiometric readout of enzyme activity (26). Notably, the CPF4 fluorescence ratio is insensitive to pH in the physiological range (pH 7.0–8.0) (26). A major advantage of fluorescence-based sensors like CPF4 is their high sensitivity, allowing detection of very low concentrations of enzyme.

We examined whether CPF4 serves as a substrate for ATX. As shown in Fig. 4*B*, ATX-Myc causes a prominent loss of FRET (increased donor fluorescence and a concomitant decrease in acceptor fluorescence), indicative of substrate hydrolysis, which can be monitored in real time (Fig. 4*C*). No CFP4 signal change was detected with the inactive mutant ATX(T210A). A plot of the initial hydrolysis rates *versus* CPF4 concentration revealed Michaelis-Menten kinetics with an average K_m as low as ~4 μM (range, 2.5–6 μM) for ATX-Myc in HEK293 cell-conditioned medium (Fig. 4*D*). About the same K_m value was found with highly purified ATX from Sf9 cell supernatant (see below and Fig. 6), suggesting that conditioned medium does not contain significant amounts of competitive inhibitors of ATX (which would increase the apparent K_m).

It is noteworthy that the apparent affinity of ATX for CPF4 is 2–3 orders of magnitude higher than that for lysophospholipids and nucleotides (K_m = 0.1–1.0 mM; one notable exception is diadenosine triphosphate with an apparent K_m of 8 μM (33)). Also with bis-pNPP, a "non-Michaelis-Menten" substrate, half-maximal hydrolysis rates are observed at concentrations as high as ~0.5 mM. Thus attachment of the coumarin-fluorescein tandem to bis-pNPP, which increases hydrophobicity and disturbs structural symmetry, converts bis-pNPP into a high-affinity substrate for ATX, suggesting that the coumarin-fluorescein tandem fits into a hydrophobic pocket involved in substrate binding. Although the overall catalytic efficiency (V_{max}/K_m) of CPF4 hydrolysis was about 3-fold lower than that observed with the other substrates, the FRET-based assay showed superior sensitivity; even at a 5000-fold dilution of HEK293T cell-conditioned medium, ATX activity was still detectable. The estimated detection limit of the CFP4 assay was 3 ng of ATX/ml, exceeding that of the standard colorimetric assay by at least 50-fold. This makes CPF4 the preferred probe for measuring ATX activity in conditioned media and body fluids, although it remains to be seen to what extent the presence of binding proteins and/or nonspecific phosphodiesterases may limit the usefulness of CPF4 in assessing ATX activity in complex biological fluids.

We also examined whether CPF4 is a substrate for nonmammalian secreted lyso-PLDs, notably the broad specificity PLD from *S. chromofuscus* and the sphingomyelin- and LPC-specific PLDs from *C. pseudotuberculosis* and *Loxosceles laeta* (28). When assayed under the conditions used for ATX, none of these exogenous PLDs (10 nM) was able to cleave CPF4 (results not shown). It thus appears that among the known secreted PLDs, only ATX can hydrolyze CPF4.

Inhibition of ATX by LPA and S1P—Because of its superior sensitivity and convenient readout, the CPF4 assay was used

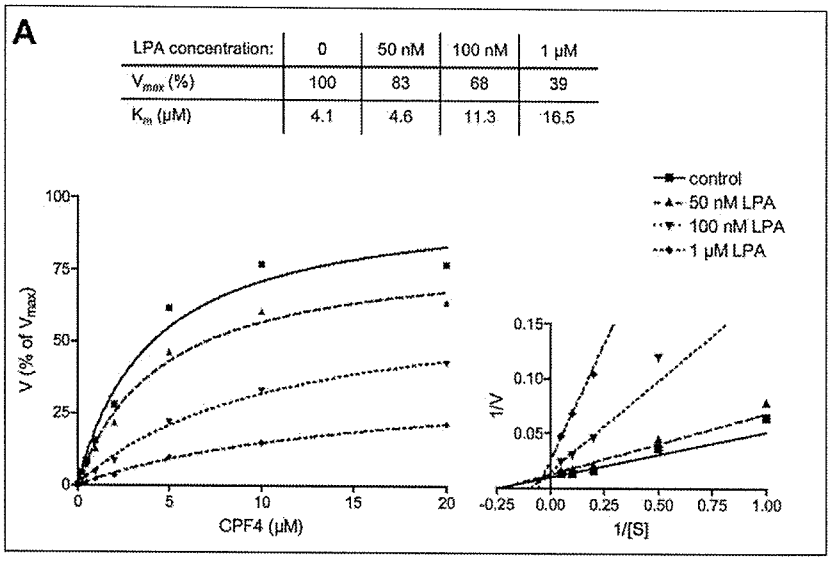

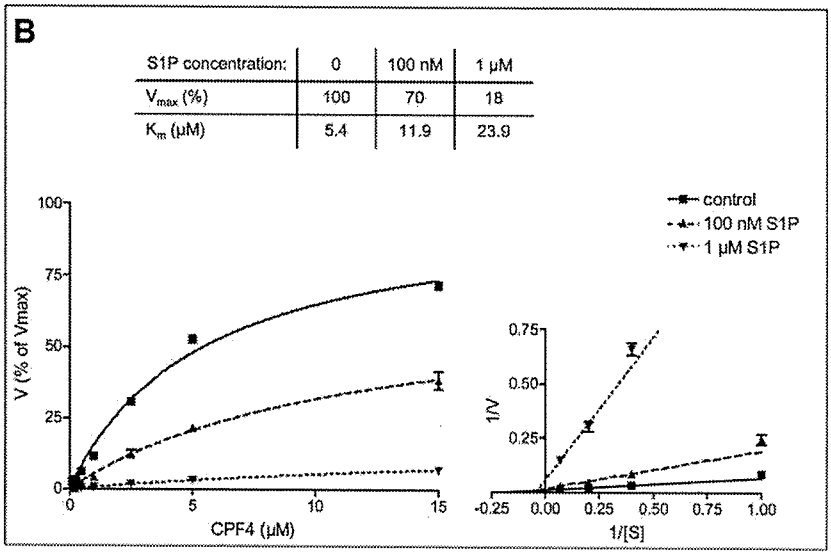

FIG. 6. **Kinetic analysis of ATX inhibition by LPA and S1P.** Inhibition of ATX-Myc by 1-oleoyl-LPA (*A*) and S1P (*B*) added at the indicated concentrations. Inhibition by LPA and S1P produces a decrease in V_{max} and an increase in K_m, indicative of "mixed-type" inhibition. Similar results were obtained with purified recombinant ATX (not shown).

in our further analysis of ATX inhibition. We determined the concentration dependence of LPA and S1P for inhibiting ATX activity using a substrate concentration close to the K_m. Under those conditions, the IC_{50} value for 1-oleoyl-LPA is ~0.1 μM (Fig. 5*A*), very similar to the value found with pNP-TMP or LPC as substrate (Fig. 3*D* and results not shown). S1P inhibited ATX activity with the same dose dependence as observed for LPA (Fig. 5*A*). Other natural lipids, including dioleoylphosphatidic acid, 1-oleoyl-glycerol, sphingosine (10 mM), glycerol 3-phosphate (1 mM), and free fatty acids, did not affect ATX activity. Although AMP has been reported to inhibit the NPP reaction (1, 2), we did not observe any effect of either AMP or ATP (1 mM) on ATX activity (results not shown).

Importantly, the inhibitory effects of LPA and S1P were specific for ATX in that the activity of the structurally related ecto-phosphodiesterase NPP1 was insensitive to either lipid (Fig. 5*A*). Inhibition of ATX by LPA was dependent on the length of the acyl chain; maximal inhibition was induced by 1-oleoyl-LPA, 1-palmitoyl-LPA, and 1-myristoyl-LPA, whereas short-chain LPA(6:0) had no measurable effect (Fig. 5*B*). The apparent requirement of a long acyl chain suggests that LPA and S1P directly interact with a hydrophobic pocket on ATX. The inhibitory effects of LPA and S1P were nonadditive (Fig. 5*B*), suggesting that both lipids act on the same regulatory site. We conclude that, in marked contrast to the G protein-coupled receptors (17), ATX does not discriminate between LPA and S1P as ligands.

We next examined the mechanism of inhibition by LPA and S1P. Substrate titration studies revealed that LPA and S1P are mixed-type inhibitors, producing a reduction in V_{max} and an increase in K_m (Fig. 6). In other words, inhibition of ATX by LPA/S1P has both a noncompetitive and a competitive compo-

nent, resulting from a combination of a decreased turnover number and decreased affinity of the active site for its substrates. Double-reciprocal plot analysis (Fig. 6) yielded an inhibition constant (K_i) of 110 nM for LPA and 50 nM for S1P, values well within the biologically active range of LPA and S1P. We note that these K_i values are ~1000-fold lower than the reported K_m for the LPC substrate (100–200 μM) (11, 12, 14), indicating that ATX binds LPA and S1P much more strongly than it binds its physiological substrate(s).

Conclusion —We have employed a novel and highly sensitive FRET-based phosphodiesterase sensor to show that the catalytic activity of ATX, secreted by the classical export pathway, is potently and specifically inhibited by LPA and S1P. Kinetic analysis revealed that LPA and S1P act as mixed-type inhibitors with an inhibition constant (K_i) of ~0.1 μM. The inhibition of ATX by LPA and S1P is specific in that (i) short-chain LPA(6:0) and other lipids have no effect, and (ii) the closely related ecto-phosphodiesterase NPP1, which lacks lyso-PLD activity, is insensitive to LPA and S1P. Because ATX primarily functions as an LPA-generating lyso-PLD, our findings imply that LPA is capable of controlling its own biosynthesis in the cellular environment. Product inhibition of ATX will prevent excessive accumulation of bioactive LPA in the extracellular milieu and may explain why steady-state plasma levels of LPA are very low despite the abundance of its precursor LPC. That serum LPA levels rapidly increase following platelet activation (24) suggests that plasma ATX may also be positively regulated by as yet unknown factors, an important issue that needs to be further explored.

Our findings point to a novel role for S1P as an inhibitor of ATX, in addition to its well documented role as a receptor agonist. The important implication is that changes in extracellular S1P levels may greatly influence LPA production and signaling. Because the S1P concentrations in blood are significant (16, 34), close to the inhibition constant for ATX reported here (~ 0.1 μM), ATX activity in plasma could be permanently suppressed by S1P under basal conditions. Our results further imply that ATX has a unique binding site for LPA and S1P, not present in NPP1. Interestingly, a photo-affinity labeling study has shown that, in addition to its catalytic site, ATX contains an isoform-specific sequence that can be cross-linked to ATP (35). Mutagenesis experiments, in combination with structural studies, should reveal whether this second nucleotide-binding region is in fact an allosteric site for LPA and S1P. Identification and characterization of the LPA/S1P binding site(s) is a major challenge for future studies and will likely facilitate the development of selective ATX inhibitors that could be of value in anticancer therapy.

Acknowledgments—We thank Ben Giepmans for help with cDNA cloning and Mary Roberts, Denise Tambourgi, and Steve Billington for purified PLDs.

REFERENCES

1. Bollen, M., Gijsbers, R., Ceulemans, H., Stalmans, W., and Stefan, C. (2000) *Crit. Rev. Biochem. Mol. Biol.* **35,** 393–432
2. Clair, T., Lee, H. Y., Liotta, L. A., and Stracke, M. L. (1997) *J. Biol. Chem.* **272,** 996–1001
3. Goding, J. W., Grobben, B., and Slegers, H. (2003) *Biochim. Biophys. Acta* **1638,** 1–19
4. Stracke, M. L., Krutzsch, H. C., Unsworth, E. J., Arestad, A., Cioce, V., Schiffmann, E., and Liotta, L. A. (1992) *J. Biol. Chem.* **267,** 2524–2529
5. Murata, J., Lee, H. Y., Clair, T., Krutzsch, H. C., Arestad, A. A., Sobel, M. E., Liotta, L. A., and Stracke, M. L. (1994) *J. Biol. Chem.* **269,** 30479–30484
6. Nam, S. W., Clair, T., Campo, C. K., Lee, H. Y., Liotta, L. A., and Stracke, M. L. (2000) *Oncogene* **19,** 241–247
7. Nam, S. W., Clair, T., Kim, Y. S., McMarlin, A., Schiffmann, E., Liotta, L. A., and Stracke, M. L. (2001) *Cancer Res.* **61,** 6938–6944
8. Mills, G. B., and Moolenaar, W. H. (2003) *Nat. Rev. Cancer* **3,** 582–591
9. Fuss, B., Baba, H., Phan, T., Tuohy, V. K., and Macklin, W. B. (1997) *J. Neurosci.* **17,** 9095–9103
10. Bachner, D., Ahrens, M., Betat, N., Schroder, D., and Gross, G. (1999) *Mech. Dev.* **84,** 121–125
11. Umezu-Goto, M., Kishi, Y., Taira, A., Hama, K., Dohmae, N., Takio, K., Yamori, T., Mills, G. B., Inoue, K., Aoki, J., and Arai, H. (2002) *J. Cell Biol.* **158,** 227–233
12. Tokumura, A., Majima, E., Kariya, Y., Tominaga, K., Kogure, K., Yasuda, K., and Fukuzawa, K. (2002) *J. Biol. Chem.* **277,** 39436–39442
13. Moolenaar, W. H., van Meeteren, L. A., and Giepmans, B. N. (2004) *BioEssays* **26,** 870–881
14. Clair, T., Aoki, J., Koh, E., Bandle, R. W., Nam, S. W., Ptaszynska, M. M., Mills, G. B., Schiffmann, E., Liotta, L. A., and Stracke, M. L. (2003) *Cancer Res.* **63,** 5446–5453
15. Postma, F. R., Jalink, K., Hengeveld, T., and Moolenaar, W. H. (1996) *EMBO J.* **15,** 2388–2392
16. Hla, T., Lee, M. J., Ancellin, N., Paik, J. H., and Kluk, M. J. (2001) *Science* **294,** 1875–1878
17. Ishii, I., Fukushima, N., Ye, X., and Chun, J. (2004) *Annu. Rev. Biochem.* **73,** 321–354
18. Liliom, K., Sun, G., Bunemann, M., Virag, T., Nusser, N., Baker, D. L., Wang, D. A., Fabian, M. J., Brandts, B., Bender, K., Eickel, A., Malik, K. U., Miller, D. D., Desiderio, D. M., Tigyi, G., and Pott, L. (2001) *Biochem. J.* **355,** 189–197
19. Spiegel, S., and Milstien, S. (2003) *Nat. Rev. Mol. Cell. Biol.* **4,** 397–407
20. Koh, E., Clair, T., Woodhouse, E. C., Schiffmann, E., Liotta, L., and Stracke, M. (2003) *Cancer Res.* **63,** 2042–2045
21. Gijsbers, R., Aoki, J., Arai, H., and Bollen, M. (2003) *FEBS Lett.* **538,** 60–64
22. Eichholtz, T., Jalink, K., Fahrenfort, I., and Moolenaar, W. H. (1993) *Biochem. J.* **291,** 677–680
23. Baker, D. L., Morrison, P., Miller, B., Riely, C. A., Tolley, B., Westermann, A. M., Bonfrer, J. M., Bais, E., Moolenaar, W. H., and Tigyi, G. (2002) *J. Am. Med. Assoc.* **287,** 3081–3082
24. Sano, T., Baker, D., Virag, T., Wada, A., Yatomi, Y., Kobayashi, T., Igarashi, Y., and Tigyi, G. (2002) *J. Biol. Chem.* **277,** 21197–21206
25. Croset, M., Brossard, N., Polette, A., and Lagarde, M. (2000) *Biochem. J.* **345,** 61–67
26. Takakusa, H., Kikuchi, K., Urano, Y., Sakamoto, S., Yamaguchi, K., and Nagano, T. (2002) *J. Am. Chem. Soc.* **124,** 1653–1657
27. Lee, H. Y., Clair, T., Mulvaney, P. T., Woodhouse, E. C., Aznavoorian, S., Liotta, L. A., and Stracke, M. L. (1996) *J. Biol. Chem.* **271,** 24408–24412
28. van Meeteren, L. A., Frederiks, F., Giepmans, B. N., Pedrosa, M. F., Billington, S. J., Jost, B. H., Tambourgi, D. V., and Moolenaar, W. H. (2004) *J. Biol. Chem.* **279,** 10833–10836
29. Stracke, M. L., Clair, T., and Liotta, L. A. (1997) *Adv. Enzyme Regul.* **37,** 135–144
30. Kelly, S. J., Dardinger, D. E., and Butler, L. G. (1975) *Biochemistry* **14,** 4983–4988
31. Rudolph, A. E., Stuckey, J. A., Zhao, Y., Matthews, H. R., Patton, W. A., Moss, J., and Dixon, J. E. (1999) *J. Biol. Chem.* **274,** 11824–11831
32. Zambonelli, C., Casali, M., and Roberts, M. F. (2003) *J. Biol. Chem.* **278,** 52282–52289
33. Vollmayer, P., Clair, T., Goding, J. W., Sano, K., Servos, J., and Zimmermann, H. (2003) *Eur. J. Biochem.* **270,** 2971–2978
34. Yang, L., Yatomi, Y., Miura, Y., Satoh, K., and Ozaki, Y. (1999) *Br. J. Haematol.* **107,** 282–293
35. Clair, T., Krutzsch, H. C., Liotta, L. A., and Stracke, M. L. (1997) *Biochem. Biophys. Res. Commun.* **236,** 449–454

Available online at www.sciencedirect.com
SCIENCE DIRECT®
Archives of Biochemistry and Biophysics 442 (2005) 222–228
ABB
www.elsevier.com/locate/yabbi

Evidence for pH dependent Zn^{2+} influx in K562 erythroleukemia cells: Studies using ZnAF-2F fluorescence and $^{65}Zn^{2+}$ uptake

Robert A. Colvin [a,*], Charles P. Fontaine [a], Dustin Thomas [a], Tomoya Hirano [b], Tetsuo Nagano [b], Kazuya Kikuchi [b]

[a] *Department of Biological Sciences, OHIO University, Athens, OH 45701, USA*
[b] *Graduate School of Pharmaceutical Sciences, The University of Tokyo, Tokyo, Japan*

Received 10 July 2005, and in revised form 17 August 2005
Available online 8 September 2005

Abstract

Using both ZnAF-2F (a Zn^{2+} specific fluorophore) and $^{65}Zn^{2+}$, we determined the rate of transporter mediated Zn^{2+} influx (presumably mediated by the SLC39A1 gene product, protein name hZIP1) under steady state conditions and studied the effects of extracellular acidification. When K562 erythroleukemia cells were placed in Zn^{2+} containing buffers (1–60 μM), the initial rate of $^{65}Zn^{2+}$ accumulation mirrored the apparent rise in free intracellular Zn^{2+} concentrations sensed by ZnAF-2F. Therefore, newly transported Zn^{2+} equilibrated with the free intracellular Zn^{2+} pool sensed by ZnAF-2F. A new steady state with elevated free intracellular Zn^{2+} was established after about 30 min. An estimate of 11 μM for the K_m and 0.203 nmol/mg/s for the V_{max} were obtained for Zn^{2+} influx. $^{65}Zn^{2+}$ uptake and ZnAF-2F fluorescent changes were inhibited by extracellular acidification (range tested: pH 8–6, IC_{50} = pH 6.34). The IC_{50} for proton effects was close to the pK_a for histidine, suggesting conserved histidine residues present in SLC39A1 play a critical role in Zn^{2+} influx and are involved in the pH effect.

Keywords: Metal ion transport; Zinc homeostasis; Fluorescence

Using currently available genomic data and analyses from several eukaryotic organisms, Zn^{2+} transporters appear to fall into two distinct gene families named SLC39 (protein name: ZIP) [1,2] and SLC30 (protein name: ZnT) [3]. Functional characterization of the mammalian SLC39 family members (hZIP-1, -2, and -4) provides convincing support for the notion that SLC39 proteins are targeted to the plasma membrane and are involved primarily in cellular Zn^{2+} influx [4–7]. SLC39 proteins appear to mediate a facilitated diffusion of Zn^{2+}, driven primarily by the concentration gradient for Zn^{2+} across the plasma membrane. No evidence exists for an energy requirement, effect of membrane potential, or the cotransport of other ions, except perhaps bicarbonate (SLC39A2 only) [4,5]. Thus, very little is known concerning the mechanism of Zn^{2+} influx. One recent study suggests that SLC39 proteins move ligand bound Zn^{2+} across the plasma membrane (rather than free Zn^{2+}) [8], the implication being that Zn^{2+} added in solution is a poor measure of the protein's true affinity for Zn^{2+}.

The function, tissue location, and mechanism of Zn^{2+} transport by SLC30 family members are best studied for the product of the mammalian gene SLC30A1 (ZnT-1) and its several homologs. [9]. SLC30A1 is ubiquitously expressed and likely to be involved in Zn^{2+} efflux. For example, PC-12 cells expressing SLC30A1 show increased Zn^{2+} efflux and reduced sensitivity to Zn^{2+} induced cell death [10]. The remaining SLC30 family members are preferentially localized to intracellular membranes where they have more limited, tissue specific expression, probably related to physiological intracellular Zn^{2+} compartmentalization [11–16]. Several studies [5,9,14–16] support a division of labor between Zn^{2+} transporters. Thus, SLC39 family members

* Corresponding author. Fax: +1 740 593 0300.
E-mail address: colvin@ohio.edu (R.A. Colvin).

0003-9861/$ - see front matter © 2005 Elsevier Inc. All rights reserved.
doi:10.1016/j.abb.2005.08.013

are responsible for Zn^{2+} influx and SLC30 family members are involved in Zn^{2+} efflux and intracellular compartmentalization. This leads to a model predicting that under steady state conditions, free intracellular Zn^{2+} concentrations are maintained by a balance between the rate of separate and distinct Zn^{2+} influx and efflux mechanisms across the plasma membrane and exchange with sequestered Zn^{2+} pools inside the cell. However, direct experimental proof of this model in mammalian cells is lacking at present.

Our laboratory is studying Zn^{2+} transport using cultured cells in hopes of addressing questions of transport mechanism and the role of mammalian Zn^{2+} transporters in cellular homeostasis. One of our consistent findings is an inhibition of $^{65}Zn^{2+}$ uptake by extracellular acidification. In addition, we have shown that intracellular acidification of cortical neurons results in a stimulation of $^{65}Zn^{2+}$ uptake [17,18]. These data have led us to hypothesize that protons are fundamental to the uptake mechanism and the pH effect could reflect an antiport mechanism of coupled Zn^{2+}/proton transport. Unfortunately, no experimental evidence exists linking protons to the transport mechanisms of either SLC30 or SLC39 family members. To address issues of cellular Zn^{2+} homeostasis and the mechanism(s) of Zn^{2+} transport, we used a model cell system (K562 erythroleukemia cells) with well characterized Zn^{2+} uptake transporter function and two complimentary techniques—ZnAF-2F fluorescence and $^{65}Zn^{2+}$ uptake. These studies allowed us to measure initial rates of Zn^{2+} influx and measure changes in steady state intracellular Zn^{2+} levels. Our data suggests that SLC39A1 (hZIP1) transport function was inhibited by extracellular acidification.

Materials and methods

Culture of K562 erythroleukemia cells

K562 erythroleukemia cells (#CCL-243) were obtained from American Type Culture Collection (Manassas, VA). Cells were maintained in complete RPMI 1640 medium (Life Technologies), supplemented with 2 mM glutamine and 10% fetal bovine serum (Atlas Biologicals, Fort Collins, CO) with 500 ng/ml Gentamicin and 250 ng/ml Fungizone (Life Technologies) added. Cells were grown in suspension in 25 cm^2 flasks at 37 °C in a 5% CO_2 incubator. When necessary, cells were allowed to attach to poly-D-lysine (0.1 mg/ml in borate buffer) coated coverslips overnight. Approximately, 5×10^4 cells were applied to each coverslip. This quantity of cells per coverslip provides an optimal fluorescent signal when using ZnAF-2F.

$^{65}Zn^{2+}$ flux measurements

Experiments were performed similar to those described previously [17]. K562 cells were first harvested by centrifugation (5 min at 500 rpm—Beckman Allegra 25R centrifuge) and then resuspended in Locke's buffer (154 mM NaCl, 5.6 mM KCl, 2.3 mM $CaCl_2$, 1.0 mM $MgCl_2$, 5 mM Hepes, and 10 mM glucose). The cell suspension was then assayed for protein by the Bio-Rad method using bovine serum albumin as the standard. The cells were then diluted to a concentration of 1.5–2.0 mg/ml. Locke's buffers (bubbled with O_2 to remove dissolved CO_2) containing $^{65}Zn^{2+}$ (Los Alamos National Laboratory, NM) were prepared by adding various amounts of 1 mM $^{65}Zn^{2+}$ (0.01–0.02 μCi/μl). Transport reactions were initiated by adding 0.225 ml of prewarmed (37 °C) buffer to .025 ml of cell suspension in a 37 °C water bath. After various times, the reaction tubes were removed from the water bath and immediately placed in ice to stop the transport reaction. Cell suspensions were rapidly filtered on GF/C filter paper using a Brandel cell harvester and washed 3 times with ice-cold buffer containing 137 mM cholineCl/10 mM Hepes, pH 7.4/1 mM EGTA. When initial velocity experiments were performed, the transport reactions were stopped by filtration. The radioactivity caught on the filters was determined by liquid scintillation counting. As total Zn^{2+} added to the buffers was known ($^{65}Zn^{2+}$ plus nonradioactive Zn^{2+}), aliquots of the uptake buffer were counted for radioactivity to determine the specific activity of $^{65}Zn^{2+}$. Using this value, the counts on the filter were converted to nanomoles of Zn^{2+} per milligram protein.

SNARF-1 fluorescence and acidification

K562 cells attached to poly-D-lysine coated glass coverslips were loaded with SNARF-1 by incubation for 30 min in Locke's buffer (pH 7.4) at 37 °C containing 5 μM 5-(and-6)-carboxy SNARF-1, acetoxymethyl ester, acetate (Molecular Probes, Eugene, OR) [17]. The cells were then washed with 1 ml of Locke's buffer prior to pH measurement. The cells were then placed on ice until being used for an experiment. Cells attached to coverslips were held in a cuvette at approximately a 45° angle to the incident light beam by a coverslip holder (Hitachi Instruments, San Jose, CA). To measure fluorescence changes, the cuvette/coverslip holder was placed in the fluorescence spectrophotometer (Hitachi F-2000). To switch buffer solutions, the coverslip and holder were lifted out of the cuvette and quickly placed into a waiting cuvette containing the next desired buffer. SNARF-1 fluorescence was measured using excitation at 514 nm and emission wavelengths of 585 and 630 nm. The fluorescence ratio F_{585}/F_{630} was calibrated in separate experiments using cells treated with 10 μM nigericin in Locke's buffer of various pH containing 120 mM KCl. Using the calibration data, intracellular pH was calculated directly from F_{585}/F_{630}. F_{585}/F_{630} was a linear function of pH over pH values between 6.4 and 8.0. In each experiment, to correct for scattered light/autofluorescence, data obtained from cells treated as above but without SNARF-1 incubation were subtracted from data obtained with SNARF-1 incubation.

ZnAF-2F fluorescence

K562 cells attached to poly-D-lysine coated glass coverslips were loaded with ZnAF-2F by incubation for 60 min in Locke's buffer (pH 7.4) at 37 °C containing 5 μM ZnAF-2F

diacetyl ester [21]. The cells were then placed in fresh Locke's buffer and incubated at 37 °C for an additional 30 min. Finally, the cells were placed on ice until used for an experiment. ZnAF-2F fluorescence changes were measured using excitation at 492 nm and emission at 524 nm. Data points were collected at various intervals and saved to a data file. Since ZnAF-2F is not a ratiometric probe, fluorescence data is presented as $\Delta F/F_0$. F_0 is the average fluorescence intensity obtained for each coverslip during a brief preincubation (20–90 s) in Locke's buffer (pH 6 or 8) without added Zn^{2+}. After preincubation, an experimental run was initiated by the addition of various solutions (e.g., Zn^{2+}, CaEDTA, and dH_2O) to the cuvette via a port in the coverslip holder. Opening the door to the cuvette chamber caused a brief disturbance in the recorded data. These data points were deleted and usually amounted to about 2–5 s of data. To calculate $\Delta F/F_0$, F_0 was subtracted from each data point ($=\Delta F$) and was normalized using F_0 ($=\Delta F/F_0$). ZnAF-2F (10 mM in DMSO) was mixed with an equal volume of pluronic acid (20% in DMSO, Molecular Probes) just before use and added with the appropriate dilution in Locke's buffer to obtain the desired final concentration for incubation with cells.

Correction for photodecay

Many experiments using ZnAF-2F required long incubations (up to 1 h), thus a correction for fluorescence changes due to photodecay was necessary. First, we determined the changes in intracellular pH occurring when cells were placed in pH 6 or 8 buffers (intracellular pH dropped from about 7.5 to about 6.7, measured with SNARF-1 fluorescence). The results can be seen in the inset to Fig. 1.

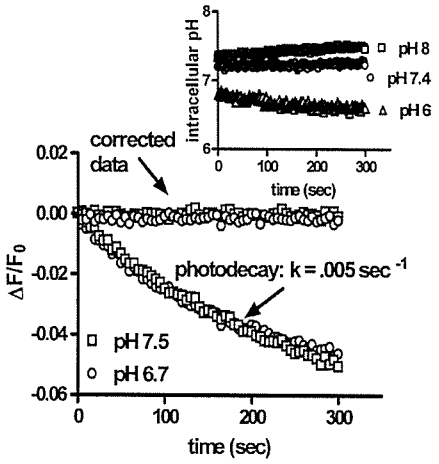

Fig. 1. Analysis of photodecay of ZnAF-2F and the effect of pH. ZnAF-2F free acid (1 μM) was added to 1 μM $ZnCl_2$ (10 mM Hepes) and then fluorescence recorded to observe the photodecay effect. Experiments were performed at either pH 7.5 or 6.7, which were intracellular pH values determined for conditions in this study. For ZnAF-2F results, data are from replicate experiments. Inset: intracellular pH was determined in K562 erythroleukemia cells preincubated with 5 μM SNARF-1 and then placed into either pH 8, 7.4, or 6 Locke's buffer. Intracellular pH was estimated as described in Materials and methods.

Fig. 1 shows that the fluorescence signal decay was fit by a one phase exponential curve. K_{decay} and span were estimated from the decay data (see Fig. 1) using non linear curve fitting (GraphPad Prism ver 4, GraphPad Software, San Diego, CA) to the equation: $y = \text{span} \cdot \exp(-K \cdot x) + \text{plateau}$. $\Delta F/F_0$ values calculated from raw data were corrected at each time point for decay using the equation: fraction remaining $= e^{-K \cdot \text{time}}$. The fraction remaining was subtracted from 1 and multiplied by the span to obtain the correction factor, which was then added to $\Delta F/F_0$ at each time point. The net effect of the correction was to level the fluorescence signal over time (see Fig. 1). No effect of pH was seen on the decay rate. As the decay rate varied slightly from experiment to experiment, each experiment was corrected with its own decay rate.

Results

Previous studies using cultured rat cortical neurons show a robust $^{65}Zn^{2+}$ uptake when cells are placed in buffers containing micromolar concentrations of $^{65}Zn^{2+}$. $^{65}Zn^{2+}$ uptake was inhibited by extracellular acidification and stimulated by intracellular acidification [17–20]. We hypothesized that proton effects are fundamental to the transport mechanism and suggested the mechanism responsible for $^{65}Zn^{2+}$ uptake in cortical neurons could be a Zn^{2+}/H^+ antiporter. In an attempt to identify the protein responsible for pH dependent Zn^{2+} uptake, we took advantage of the well characterized pH dependence of plasma membrane Zn^{2+} transport in cortical neurons to examine the pH dependence of the SLC39A1 protein. The SLC39A1 protein is a logical choice since the kinetic properties of $^{65}Zn^{2+}$ uptake in cortical neurons [17], mirror closely those of the SLC39 family of transporters [4,5]. To test the hypothesis that the SLC39A1 protein (the gene is expressed in the brain) mediates pH dependent $^{65}Zn^{2+}$ uptake, we studied K562 erythroleukemia cells. Importantly, antisense oligonucleotides directed against SLC39A1 expression show nearly complete inhibition of $^{65}Zn^{2+}$ uptake indicating that SLC39A1 expression is sufficient to account for endogenous $^{65}Zn^{2+}$ uptake in K562 cells [5].

The net accumulation of $^{65}Zn^{2+}$ in K562 erythroleukemia cells is inhibited by extracellular acidification

Fig. 2 shows the dependence of the initial velocity of $^{65}Zn^{2+}$ uptake at pH 8 on extracellular Zn^{2+} concentration. The data were fit to a rectangular hyperbola ($y = V_{max} \cdot x)/(K_m + x)$ using GraphPad Prism (ver 4) yielding estimates of 11 μM for the K_m and 0.203 nmol/mg/s for the V_{max}. The inset to Fig. 2 shows that linear uptake is observed at least over the first 20 s at 30 μM extracellular Zn^{2+}added. This is the amount of extracellular Zn^{2+} used in subsequent experiments. However, uptake did not extrapolate to zero uptake at zero time, but to about 0.8 nmol/mg. Zero time uptake was estimated by mixing ice cold cells with ice cold reaction buffer and immediately filtering the mix. The value obtained (0.78 nmol/mg at 30 μM extracellular Zn^{2+}) matched the

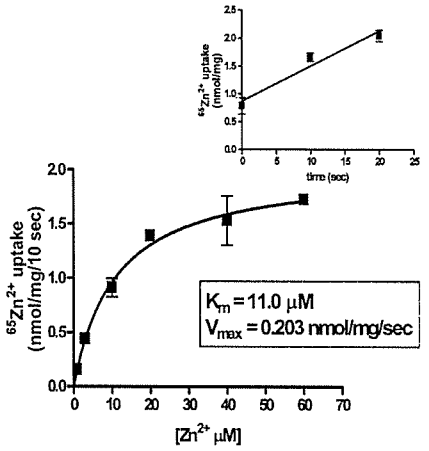

Fig. 2. Concentration dependence of the initial velocity of $^{65}Zn^{2+}$ uptake. K562 erythroleukemia cells were incubated at 37 °C with either 1, 3, 10, 20, 40, or 60 μM $^{65}Zn^{2+}$ added, for 10 s. The reaction was stopped by immediately filtering the cell suspension followed with three washes of ice cold EGTA wash buffer (see Materials and methods). Inset: cells were treated as described above in 30 μM $^{65}Zn^{2+}$ for either 10 or 20 s before stopping the reaction. Zero time was estimated by mixing ice cold cells with ice cold buffer (30 μM $^{65}Zn^{2+}$) and immediately filtering. Each point represents the mean ± SEM of three replicate experiments.

extrapolated zero value, as can be seen in the inset. Zero time $^{65}Zn^{2+}$ uptake most likely represents plasma membrane bound and residual $^{65}Zn^{2+}$ caught on the filters that is resistant to removal by the cold wash buffer. This interpretation was confirmed when comparing $^{65}Zn^{2+}$ uptake data with ZnAF-2F fluorescence changes (see Fig. 4).

Figs. 3A and B show that during its initial phase, total $^{65}Zn^{2+}$ uptake was inhibited as much as 60% by changing the extracellular pH from 8 to 6, an effect similar to that seen in cortical neurons [17]. As a control (see Fig. 3A), it is shown that the inclusion of 1 mM CaEDTA completely inhibits $^{65}Zn^{2+}$ uptake (1 mM CaEDTA is typically used to chelate free extracellular Zn^{2+} because EDTA has a much higher affinity for Zn^{2+} than Ca^{2+}. Thus, free Zn^{2+} is lowered to picomolar levels, whereas free Ca^{2+} is barely affected.). The pH dependence of the initial uptake velocity shows a smooth monophasic curve with an IC_{50} (pH 6.34) estimated from non linear curve fitting (GraphPad Prism ver 4). These data suggest that SLC39A1 protein transport function was inhibited by lowering extracellular pH.

In the presence of elevated extracellular Zn^{2+}, K562 erythroleukemia cells establish a new steady state with elevated free intracellular Zn^{2+}, shown with studies using the cell permeable fluorophore, ZnAF-2F DA, and $^{65}Zn^{2+}$

ZnAF-2F DA is a membrane permeable fluorophore with high affinity for Zn^{2+}, little pH sensitivity, and excellent selectivity over other divalent cations [21]. Fig. 4 shows fluorescence changes observed in K562 cells containing ZnAF-2F after addition of 30 μM Zn^{2+} compared to cells after an equal volume of water was added. When extracellular Zn^{2+} was increased a rising curvilinear trace was obtained, consistent with increasing intracellular free Zn^{2+} (see Fig. 4A). Intracellular free Zn^{2+} appeared to increase gradually until a new steady state was established, approximately 30 min after addition of Zn^{2+}.

As shown above, when K562 cells are placed in Zn^{2+} containing buffers, they accumulate significant amounts of $^{65}Zn^{2+}$ and show detectable ZnAF-2F fluorescence changes because of increased influx, but what is the relationship between these two measurements? Cellular Zn^{2+} content is determined by the relative rates of Zn^{2+} influx and efflux. When Zn^{2+} influx increases one expects an increase in cellular Zn^{2+} content. Conversely, when Zn^{2+} efflux increases, cellular Zn^{2+} content should decrease. When a steady state in free intracellular Zn^{2+} exists, influx and efflux are balanced and total cellular Zn^{2+} remains constant. In studies using ZnAF-2F, fluorescence changes are reporting changes in the free or easily exchangeable pools of intracellular Zn^{2+}. In studies using $^{65}Zn^{2+}$, changes in cellular $^{65}Zn^{2+}$ content can reflect plasma membrane binding, net uptake of $^{65}Zn^{2+}$, and equilibration of radioisotope with nonradioactive Zn^{2+} inside the cell (a reflection of $^{65}Zn^{2+}$/Zn^{2+} exchange). We have shown that, after placing K562 cells in buffers containing micromolar added Zn^{2+}, influx is immediately increased. A net accumulation of Zn^{2+} occurs

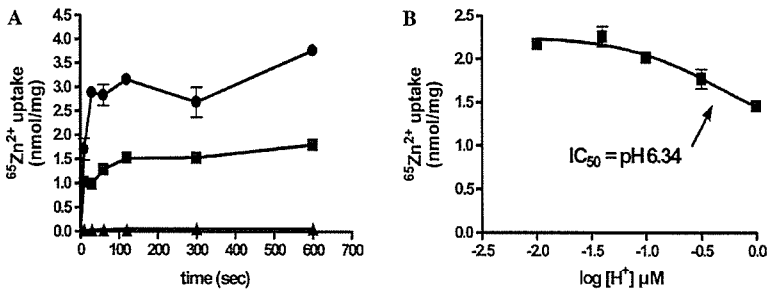

Fig. 3. Effect of pH and Zn^{2+} chelation by EDTA on $^{65}Zn^{2+}$ uptake measured in K562 erythroleukemia cells. (A) K562 erythroleukemia cells were incubated with 30 μM $^{65}Zn^{2+}$ for various times at pH 8 (●), pH 6 (■), or pH 8 containing 1 mM CaEDTA (▲). (B) Uptake reactions were performed in buffer containing 30 μM $^{65}Zn^{2+}$ adjusted to various pH values between 8 and 6. $^{65}Zn^{2+}$ uptake reactions were stopped after 10 s at 37 °C. Data were fit to the equation: y = bottom + (top−bottom)/1 + 10^(x−log IC_{50}) to estimate IC_{50} (GraphPad Prism ver 4). All data points are the means ± SEM of at least three replicate experiments.

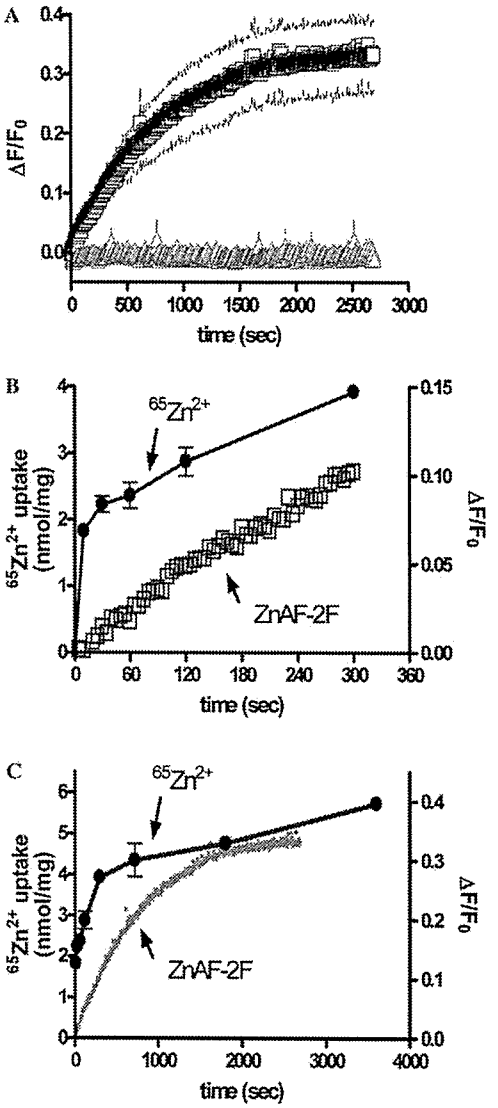

Fig. 4. ZnAF-2F fluorescence changes observed in K562 erythroleukemia cells exposed to increased extracellular Zn^{2+}. K562 erythroleukemia cells attached to glass coverslips were loaded with ZnAF-2F by incubation for 60 min in Locke's buffer (pH 7.4) at 37 °C containing 5 μM ZnAF-2F diacetyl ester. (A) Fluorescence intensity measured after either 30 μM Zn^{2+} (□), or an equal volume of water (△) was added to cells incubating in Locke's buffer pH 8 at 37 °C. Each point represents the means ± SEM (SEM represented as dotted line above and below the data points) of three replicate experiments. (B) Data from (A) (□) are plotted on the same graph with data presented in Fig. 3A—$^{65}Zn^{2+}$ uptake in the presence of 30 μM $^{65}Zn^{2+}$, pH 8 (●). (C) Similar to (B) except data are plotted over a longer time frame (□).

resulting in increasing $^{65}Zn^{2+}$ content and changes in ZnAF-2F fluorescence. Fig. 4B shows that during the initial phase of Zn^{2+} uptake the changes in ZnAF-2F fluorescence and $^{65}Zn^{2+}$ content parallel each other, but differ in that an initial rapid accumulation of $^{65}Zn^{2+}$ is seen. Analysis of initial rates of $^{65}Zn^{2+}$ uptake (Fig. 2) suggests that the initial burst in $^{65}Zn^{2+}$ accumulation is plasma membrane/filter binding. The results of Fig. 4B agree with this interpretation. The transport reaction proceeds until a new steady state is attained (see Fig. 4C), as shown by both ZnAF-2F and $^{65}Zn^{2+}$ data. However, cellular $^{65}Zn^{2+}$ content will slowly continue to increase until the specific activity of $^{65}Zn^{2+}$ inside and outside the cell reaches equilibration, but likely results in little net change in cellular Zn^{2+} content.

The possibility exists that the plateau in ZnAF-2F fluorescence results from saturation or leakage of the dye, not establishment of a new steady state. We wanted to show that the leakage was in fact small and that the robustness of the intracellular dye response was well maintained even after long incubations. To show this, we used a Zn^{2+} ionophore (sodium pyrithione, −50 μM with 30 μM Zn^{2+} added) added either at the start of a reaction or after a steady state had been achieved to maximally load the cells with Zn^{2+}. It can be seen in Fig. 5 that addition of sodium pyrithione results in a large and rapid rise in ZnAF-2F fluorescence when added at the start of the reaction, in response to a large influx of Zn^{2+}. After addition of 30 μM Zn^{2+} alone a new steady state was established, however, addition of sodium pyrithione disturbed this steady state by allowing a rapid influx of additional Zn^{2+}, observed as increased ZnAF-2F fluorescence similar to that seen after addition at the start of the reaction. Thus, the establishment of a new steady state after addition of Zn^{2+}, reflected as a steady level of ZnAF-2F fluorescence, did represent a steady state in intracellular free Zn^{2+} concentration and was not the result of fluorophore saturation or leakage from the cell.

Extracellular acidification inhibits Zn^{2+} influx

In Figs. 6A and B, the effects of extracellular acidification on ZnAF-2F fluorescence changes, with or without Zn^{2+} addition are shown. We saw that the initial rate of

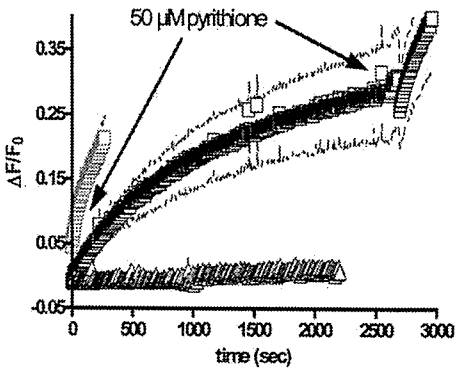

Fig. 5. ZnAF-2F fluorescence changes observed in K562 cells exposed to sodium pyrithione. K562 erythroleukemia cells attached to glass coverslips were prepared as described in the legend to Fig. 4 (30 μM Zn^{2+} added to start the reaction □; or an equal volume of water △). At the indicated times, (see arrows), 50 μM sodium pyrithione was added (pyrithione was not added to the water run). Data are means ± SEM (SEM represented as dotted line above and below the data points) of three replicate experiments.

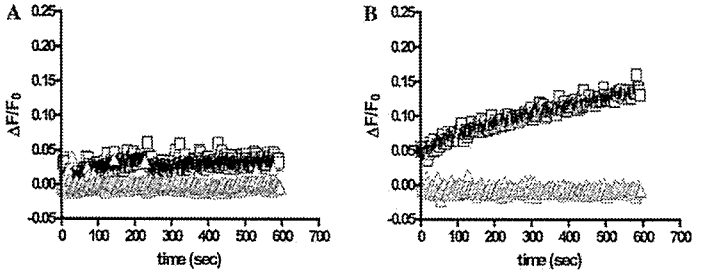

Fig. 6. ZnAF-2F fluorescence changes observed in K562 erythroleukemia cells exposed to extracellular acidification. K562 erythroleukemia cells attached to glass coverslips were prepared as described in the legend to fig. 4. (A) Cells were placed into pH 6 Locke's buffer and at time zero 30 μM Zn^{2+} (□) or an equal volume of water (△) was added. (B) Same as in (A) except that cells were in pH 8 Locke's buffer. All data represent means of at least duplicate experiments.

fluorescence increase observed after addition of 30 μM Zn^{2+} in pH 8 (see Fig. 6B), was almost completely blocked in pH 6 and differed little from that seen in the absence of added Zn^{2+} in either pH 8 or 6 (see Fig. 6A). We conclude that Zn^{2+} influx is inhibited (even in the presence of micromolar added extracellular Zn^{2+}) by extracellular acidification. Since the SLC39A1 protein is the primary, if not only, mediator of Zn^{2+} influx in K562 cells, we must conclude that SLC39A1 transport function is inhibited by extracellular acidification.

Discussion

The findings reported here demonstrate the effectiveness of using ZnAF-2F to monitor changes in intracellular Zn^{2+} and provide consistent evidence that Zn^{2+} influx in K562 erythroleukemia cells was inhibited by extracellular acidification. Our data shows that short term steady state levels of free intracellular Zn^{2+} are largely determined by the relative rates of Zn^{2+} influx and efflux across the plasma membrane. Our data is consistent with distinct pathways for Zn^{2+} influx (SLC39A1 protein mediated) and efflux. We show that under resting conditions, in Locke's buffer, K562 cells maintain a steady state with both Zn^{2+} influx (and presumably efflux) so small as to be undetectable by the methods employed in this study. Zn^{2+} influx is likely small because the contaminating concentration of free Zn^{2+} in Locke's buffer is below the activation level required to stimulate Zn^{2+} influx. Adding micromolar amounts of Zn^{2+} to the Locke's buffer clearly stimulated Zn^{2+} influx. Efflux is small under these conditions because free intracellular Zn^{2+} is small as well.

When Zn^{2+} influx was stimulated, cellular Zn^{2+} rose, and presumably free intracellular Zn^{2+} rose until a new steady state was attained. This study provides evidence that transported $^{65}Zn^{2+}$ readily equilibrated with free intracellular Zn^{2+}. We showed that over relatively short periods of time (up to one hour in this study) free intracellular Zn^{2+} was allowed to increase in response to changes in Zn^{2+} influx. Presumably, under either physiological or pathological conditions, if Zn^{2+} were released from intracellular sequestration sites, a transient rise in free intracellular Zn^{2+} would occur also. Such a rise in free intracellular Zn^{2+} has been shown to occur in neurons after oxidative stress [22,23]. On the other hand, it is thought that long term cellular Zn^{2+} status and presumably free intracellular Zn^{2+} concentrations are regulated by the altered expression of SLC30A1 (Zn^{2+} efflux) and metallothionein [24,25] and the cycling of SLC39 proteins (Zn^{2+} influx) between the *trans*-Golgi network and the plasma membrane [6,26].

But does a free pool of intracellular Zn^{2+} even exist in eukaryotic cells? O'Halloran and co-workers [27,28] make the convincing argument that at least in *Escherichia coli*, metal binding proteins are so effective as to lower free intracellular Zn^{2+} and other metals to femtomolar levels. In eukaryotic cells, glutathione, and free amino acids (e.g., histidine) can act as additional Zn^{2+} binding moieties in addition to metallothionein/thionein pair [29,30]. Although these compounds have low affinity for Zn^{2+}, they exist in millimolar concentrations in the cell and are predicted to lower free intracellular Zn^{2+} to negligible levels. Thus, the Zn^{2+} signal sensed by ZnAF-2F might actually exist as a freely exchangeable (low affinity, bound) pool of Zn^{2+}, such that free Zn^{2+} actually changes little or not at all in our experiments.

This study adds to our growing knowledge of the transport mechanism of SLC39 proteins. SLC39 proteins are responsible for influx and appear to function by facilitated transport, dependent on a concentration gradient to provide the free energy for net movement of Zn^{2+} into the cell. This study provides evidence that SLC39A1 protein transport function is inhibited by extracellular acidification. The pH dependence of SLC39A1 protein transport activity has not been extensively studied [4,5], although the SLC39A2 protein was shown to be activated by bicarbonate ion. We took great care to eliminate bicarbonate effects by using bicarbonate free buffers bubbled with O_2. Thus, we conclude that SLC39A1 protein transport activity is inhibited by extracellular acidification and this effect is not mediated through changes in bicarbonate ion. The IC_{50} of the pH effect is remarkably close to the amino acid histidine ($pK_a = 6.0$), suggesting histidine residues in the protein could play a critical role in the mechanism of pH effects. Sequence analysis of the SLC30 gene family [1] reveals a highly conserved histidine rich domain in the large intracellular loop between

transmembrane domains III and IV (albeit the function of this loop is unclear at present). In addition, transmembrane domains IV–V, which are predicted to be involved in Zn^{2+} translocation, contain histidine residues also. Thus, conserved histidine residues present in SLC39A1 that play a critical role in Zn^{2+} influx may be involved in the pH effect. Finally, it appears likely that the previously reported pH effect on Zn^{2+} transport in cortical neurons [17] is mediated through SLC39A1 protein activity.

Acknowledgments

This work was supported by a grant from the National Institute on Aging and the Provost's Undergraduate Research Fund at OHIO University.

References

[1] D.J. Eide, Pflugers Arch. 447 (2004) 796–800.
[2] L.A. Gaither, D.J. Eide, BioMetals 14 (2001) 251–270.
[3] R.D. Palmiter, L. Huang, Pflugers Arch. 447 (2004) 744–751.
[4] L.A. Gaither, D.J. Eide, J. Biol. Chem. 276 (2001) 22258–22264.
[5] L.A. Gaither, D.J. Eide, J. Biol. Chem. 275 (2000) 5560–5564.
[6] B.E. Kim, F. Wang, J. Dufner-Beattie, G.K. Andrews, D.J. Eide, M.J. Petris, J. Biol. Chem. 279 (2004) 4523–4530.
[7] K. Wang, B. Zhou, Y.M. Kuo, J. Zemansky, J.A Gitschier, Am. J. Hum. Genet. 71 (2002) 66–73.
[8] R.B. Franklin, J. Ma, J. Zou, Z. Guan, B.I. Kukoyi, P. Feng, L.C. Costello, J. Inorg. Biochem. 96 (2003) 435–442.
[9] R.D. Palmiter, S.D. Findley, EMBO J. 14 (1995) 639–649.
[10] A.H. Kim, C.T. Sheline, M. Tian, T. Higashi, R.J. McMahon, R.J. Cousins, D.W. Choi, Brain Res. 886 (2000) 99–107.
[11] L. Huang, C.P. Kirschke, J. Gitschier, J. Biol. Chem. 277 (2002) 26389–26395.
[12] T. Kambe, H. Narita, Y. Yamaguchi-Iwai, J. Hirose, T. Amona, N. Sugiura, R. Sasaki, K. Mori, J. Biol. Chem. 277 (2002) 19049–19055.
[13] S.L. Kelleher, B. Lonnerdal, J. Nutr. 132 (2002) 3280–3285.
[14] C.P. Kirschke, L. Huang, J. Biol. Chem. 278 (2003) 4096–4102.
[15] R.D. Palmiter, T.B. Cole, S.D. Findley, EMBO J. 15 (1996) 1784–1791.
[16] R.D. Palmiter, T.B. Cole, C.J. Quaife, S.D. Findley, Proc. Natl. Acad. Sci. USA 93 (1996) 14934–14939.
[17] R.A. Colvin, Am. J. Physiol. Cell Physiol. 282 (2002) C317–C329.
[18] R.A. Colvin, N. Davis, R.W. Nipper, P.A. Carter, Neurochem. Int. 36 (2000) 539–547.
[19] R.A. Colvin, Neurosci. Lett. 247 (1998) 147–150.
[20] R.V. Balaji, R.A. Colvin, Neurochem. Res. 30 (2005) 171–176.
[21] T. Hirano, K. Kikuchi, Y. Urano, T. Nagano, J. Am. Chem. Soc. 124 (2002) 6555–6562.
[22] E. Aizenman, A.K. Stout, K.A. Hartnett, K.E. Dineley, B. McLaughlin, I.J. Reynolds, J. Neurochem. 75 (2000) 1878–1888.
[23] E. Bossy-Wetzel, M.V. Talantova, W.D. Lee, M.N. Scholzke, A. Harrop, E. Mathews, T. Gotz, J. Han, M.H. Ellisman, G.A. Perkins, S.A. Lipton, Neuron 41 (2004) 351–365.
[24] S.J. Langmade, R. Rauind, P.J. Daniels, G.K. Andrews, J. Biol. Chem. 275 (2000) 34803–34809.
[25] G.K. Andrews, Biochem. Pharmacol. 59 (2000) 95–104.
[26] F. Wang, J. Dufner-Beattie, B.E. Kim, M.J. Petris, G.K. Andrews, D.J. Eide, J. Biol. Chem. 279 (2004) 24631–24639.
[27] L.A. Finney, T.V. O'Halloran, Science 300 (2003) 931–936.
[28] C.E. Outten, T.V. O'Halloran, Science 292 (2001) 2488–2492.
[29] A. Krezel, J. Wojcik, M. Maciejczyk, W. Bal, W. May, Chem. Commun. (Camb.) 6 (2003) 704–705.
[30] W. Maret, J. Nutr. 133 (2003) 1460S–1462S.

Available online at www.sciencedirect.com
SCIENCE DIRECT
ELSEVIER
Analytical Biochemistry 350 (2006) 196–201
ANALYTICAL BIOCHEMISTRY
www.elsevier.com/locate/yabio

Detection of oxidative stress-induced mitochondrial DNA damage using fluorescence correlation spectroscopy

Yasutomo Nomura [a,*], Hirobumi Fuchigami [b], Hiroaki Kii [c], Zhonggang Feng [b], Takao Nakamura [a], Masataka Kinjo [c]

[a] *Department of Environmental Life Science, Graduate School of Medical Science, Yamagata University, Yonezawa, Yamagata 992-8510, Japan*
[b] *Department of Bio-System Engineering, Faculty of Engineering, Yamagata University, Yonezawa, Yamagata 992-8510, Japan*
[c] *Laboratory of Supramolecular Biophysics, Research Institute for Electronic Science, Hokkaido University, Sapporo 060-0812, Japan*

Received 5 September 2005
Available online 25 January 2006

Abstract

Using fluorescence correlation spectroscopy (FCS), we tested the feasibility of rapid detection of oxidative damage of mitochondrial DNA (mtDNA) in a small volume. The complete mtDNA genome was amplified by long polymerase chain reaction (LPCR), and the product was fluorescently labeled with an intercalating dye, YOYO-1. The fluorescence autocorrelation function was analyzed using a simple two-component model with the diffusion time of 0.21 ms for the LPCR primer and 18 ms for the mtDNA LPCR product. When human embryonic kidney 293 (HEK-293) cells were exposed to 0.4 mM H_2O_2, the fraction of the mtDNA LPCR product decreased significantly. In contrast, the fraction of the nuclear-encoded β-globin LPCR product remained unchanged. The analysis time of FCS measurement was very short (5 min) compared with that of gel electrophoresis (3 h). Thus, FCS allowed the rapid detection of the vulnerability of mtDNA to oxidative stress within a small volume element at the subfemtoliter level in solution. These results suggest that the LPCR–FCS method can be used for epidemiological studies of diseases caused by mtDNA damage.

Keywords: Fluorescence correlation spectroscopy; Long PCR; Mitochondria; Oxidative stress

Damaged mitochondrial DNA (mtDNA)[1] has been reported to be involved in a variety of human diseases, including diabetes, cancer, Parkinson's disease, and Alzheimer's disease [1,2]. However, the factors responsible for the damage in the diseases remain to be determined. Major candidates for the primary source of damage may be reactive oxygen species (ROS). Mitochondria produce ROS during normal respiration but can metabolize them only partially. Despite the defense system, mtDNA is particularly vulnerable because it is partially associated with the inner mitochondrial membrane [3,4].

So far, damage in mtDNA has been detected by some common methods such as Southern blotting [5] and HPLC–electrochemical detection [6]. However, one disadvantage of these techniques is that they require large quantities of mtDNA and nuclear DNA. Furthermore, because of the cost of sample preparations and the long analysis time of several hours, the techniques might not be suitable for a large-scale epidemiological study of mtDNA damage caused by oxidative stress.

To overcome these disadvantages, we propose a new methodology combining fluorescence correlation spectroscopy (FCS) with long polymerase chain reaction (LPCR). The LPCR used in the current study quantitatively amplifies the entire intact mtDNA genome alone in a small sample [7]. This technique is based on the premise that DNA

* Corresponding author. Fax: +81 238 26 3357.
E-mail address: ynomura@yz.yamagata-u.ac.jp (Y. Nomura).

[1] *Abbreviations used:* mtDNA, mitochondrial DNA; ROS, reactive oxygen species; FCS, fluorescence correlation spectroscopy; LPCR, long polymerase chain reaction; HEK-293, human embryonic kidney 293; DMEM, Dulbecco's modified Eagle's medium; PBS, phosphate-buffered saline.

0003-2697/$ - see front matter © 2006 Elsevier Inc. All rights reserved.
doi:10.1016/j.ab.2006.01.010

lesions, including those caused by oxidative damage such as strand breaks, base modification, and abasic sites, will block the progression of the polymerase, resulting in a decrease in amplification of the intact mitochondrial genome.

FCS sensitively measures fluctuations in fluorescence intensity generated by only a few fluorescent molecules diffusing in and out of an extremely tiny volume element at the subfemtoliter level in solution. The characteristics of the fluctuations are dependent on the base length and the concentration [8–10]. Thus, FCS probably detects a decrease in the LPCR product, which has the same base length as intact mtDNA. Furthermore, because of the short analysis time and the economic efficiency of the small sample volume, FCS would be advantageous for massive specimen analysis [9].

The purpose of this study was to test the feasibility of detecting mtDNA damage caused by oxidative stress using the LPCR–FCS method. After human embryonic kidney 293 (HEK-293) cells, used as test cells, were treated with different concentrations of H_2O_2 for 60 min, total cellular DNA was extracted. The mtDNA genome was amplified by LPCR and the product was confirmed with restriction enzymes. We added the fluorescent dye YOYO-1 to the LPCR medium to detect fluorescence fluctuations resulting from both the LPCR products and primer. Fluorescence autocorrelation functions were analyzed using a two-component model, and the optimal amount of template DNA was determined first. Then the dependence of the fraction of the LPCR product on H_2O_2 was evaluated.

Materials and methods

Cell culture

HEK-293 cells were grown in a 5% CO_2 humidified atmosphere at 37 °C in Dulbecco's modified Eagle's medium (DMEM) supplemented with 10% fetal bovine serum, 2×10^5 U/L penicillin G, and 200 mg/L streptomycin sulfate. The cells were routinely split every 3–4 days, and 10^6 cells were plated in 60-mm dishes 14–16 h before exposure to 0–0.4 mM H_2O_2 for 60 min [1]. Then the cells were washed once with phosphate-buffered saline (PBS) and harvested immediately by brief trypsinization (0.25%).

DNA isolation and LPCR

Using a GeneBall DNA isolation kit (TaKaRa, Japan), 30 μg of total cellular DNA was extracted from 10^6 cells. The concentration of total cellular DNA was determined by absorption at 260 nm with a SmartSpec 3000 spectrophotometer (Bio-Rad, USA). The primer nucleotide sequences were as follows: for the 16.2-kb fragment of the mitochondrial genome, the forward primer 5′-TGAG GCCAAATATCATTCTGAGGGGC-3′ and the reverse primer 5′-TTTCATCATGCGGAGATGTTGGATGG-3′ [7]; for the 17.6-kb fragment upstream of the nuclear β-globin gene (GenBank, NG_000007), the forward primer 5′-TGCACCTGCTCTGTGATTATGACTATCCCACA GTC-3′ and the reverse primer 5′-ACATGATTAGCA AAAGGGCCTAGCTTGGACTCAGA-3′. The β-globin gene encoded in the nuclear chromosome was used as a control to confirm mtDNA-specific damage.

LPCR were performed in a PC707 thermal cycler (Astec, Japan) using a TaKaRa LA Taq PCR kit as described by the manufacturer. The thermal cycle profile was as follows: initial denaturation for 1 min at 94 °C, followed by 20 cycles for mtDNA or 24 cycles for β-globin at 94 °C denaturation for 30 s and 68 °C primer extension for 15 min. A final extension at 72 °C was performed for 10 min at the completion of each profile. To confirm the LPCR product, parts of the product were digested with four restriction enzymes: *Eco*47I (TaKaRa), *Hae*III (TaKaRa), *Hga*I (New England BioLabs, USA), and *Bsp*MI (New England BioLabs). Each digest was analyzed on gel.

Fluorescence spectra of YOYO-1

The fluorescent cyanine dye YOYO-1 was purchased from Molecular Probes (USA). LPCR product–YOYO-1 complexes were made by mixing equal volumes of LPCR medium and 1 μM YOYO-1 in 10 mM Tris (pH 7.4). The mixed solution was incubated at room temperature for 30 min before use. Fluorescence spectra of YOYO-1 solution (0.5 μM) were recorded with an FP6500 fluorescence spectrophotometer (Jasco, Japan).

FCS measurement

FCS measurement was performed using a ConfoCor fluorescence correlation measurement system (Carl Zeiss Jena, Germany), as described elsewhere [11]. A sample droplet (20 μl) was set on a cover glass and was excited with approximately 10 kW/cm^2 of laser power (Ar^+) at 488 nm. The fluorescence signal was detected through a dichroic mirror (>510 nm) and a bandpass filter (515–560 nm). Measurements were conducted at room temperature.

Theoretical works on fluorescence correlation spectroscopy have been published previously by various authors [12–14]. Briefly, because fluorescence intensity fluctuates with only a few fluorescent molecules diffusing in and out of the volume element, the fluorescence intensity at time t, $I(t)$, changes into $I(t+\tau)$ τ seconds later. The fluorescence autocorrelation function is calculated from a random fluctuation of fluorescence intensity as follows:

$$G(\tau) = \frac{\langle I(t) \times I(t+\tau) \rangle}{\langle I(t) \rangle^2}. \quad (1)$$

The typical shape of an autocorrelation in Eq. (1) usually has high amplitude for time ranges shorter than approximately 1 ms and almost no amplitude for time ranges longer than approximately 1 ms. This suggests that every molecule that gives a correlation signal occupies the

volume element for a shorter time but that only a few molecules stay for a longer time. Therefore, a high amplitude lasts when large molecules stay in the volume element for a longer time because they diffuse slowly.

In the current study, the fluorescence autocorrelation function, $G(\tau)$, was fitted to a simple two-component model, where the variables were the average number of fluorescent molecules (N), the translational diffusion time of the free fast-moving component of the primer (τ_{primer}), and the translational diffusion time of the slow-moving component of the LPCR product ($\tau_{product}$), as shown in the following equation:

$$G(\tau) = 1 + \frac{1}{N}\left[\left\{\frac{1-y}{1+\frac{\tau}{\tau_{primer}}}\sqrt{\frac{1}{1+\frac{s^2\tau}{\tau_{primer}}}}\right\} + \left\{\frac{y}{1+\frac{\tau}{\tau_{product}}}\sqrt{\frac{1}{1+\frac{s^2\tau}{\tau_{product}}}}\right\}\right], \quad (2)$$

where $\tau_{primer,product} = w_0^2/4D_{primer,product}$, $s = w_o/z_o$, y is the fraction of the slow-moving component, w_o is the radius of the detection field (volume element), $2z_o$ is the field length, D_{primer} and $D_{product}$ are the translational diffusion constants of the free fast-moving product and the slow-moving product, respectively, and s is the structure parameter. The data analysis was performed using the nonlinear least-squares fitting method with the FCS ACCESS computer program (EVOTEC BioSystems, Germany). In the current study, s (0.192) was obtained previously with rhodamine 6G as the reference standard. After determining τ_{primer} and $\tau_{product}$ (see Results and discussion later), y and N were obtained from the fitting of every autocorrelation function.

The optimal amount of template DNA was determined first, and then the effect of H_2O_2 exposure on DNA damage was evaluated by changes in fraction in FCS measurement of LPCR products for mtDNA and the β-globin gene. The results were compared with those obtained by gel electrophoresis.

Frequency of DNA lesions

Assuming a random distribution of lesions, the Poisson equation (e^{-s}, where s = lesion frequency) was used to calculate the lesion frequency per genomic strand: $s = -\ln(A_d/A_o)$ = lesion frequency/strand, where A_o = the fraction of the slow component obtained from a given amount of nondamaged DNA template and A_d = the fraction of slow component of the DNA template damaged by a particular dose of H_2O_2 [15].

Densitometric analysis after gel electrophoresis

After the LPCR mixture was applied to 1% agarose gel, the gel was stained with fluorescence dye (Gelstar, TaKaRa). Then the digital image of the gel was recorded with a CCD camera (C-3040, Olympus, Japan) under UV light. The relative abundance of the LPCR product in each sample on gel was quantified by densitometric analysis using Scion Image (Scion, USA). After background subtraction, the intensities in the band of interest were divided by the highest band intensity in each gel, and the abundance was expressed as relative band intensity.

Statistical analysis

The results were analyzed for statistical significance by the unpaired Student's t test using Microcal Origin (OriginLab, USA). Values are expressed as the means and standard errors of three to five individual experiments unless stated otherwise.

Results and discussion

LPCR products labeled with YOYO-1

Using total DNA extracted from normal cells without H_2O_2 treatment, the mtDNA genome and target sequence of β-globin were amplified by LPCR. Both products were electrophoresed and appeared as single bands near 17 kbp on the gel. These were confirmed by the digestion with four restriction enzymes, demonstrating a pattern of fragment distribution identical to that expected from the GenBank data (data not shown).

In 0.5 μM YOYO-1 solution containing the mtDNA LPCR product, intense fluorescence was observed near 510 nm, as shown in Fig. 1A. YOYO-1 alone had little fluorescence at that wavelength. When interacted with the primer for mtDNA amplification, it had weak fluorescence that was one-third the fluorescence intensity of the coexistent solution of the mtDNA LPCR product. The fluorescence spectra and the intensity of the primer for the β-globin gene and of the LPCR product were identical to those for mtDNA (data not shown). Thus, the interaction between each LPCR primer and YOYO-1 also caused fluorescence.

Diffusion time of primer and LPCR products

The fluorescence autocorrelation functions of the primer for mtDNA amplification, the LPCR products for mtDNA, and the β-globin gene are shown in Fig. 1B. The function of the mtDNA LPCR product was nearly identical to that of the β-globin LPCR product due to similar base length but was largely shifted to the right compared with that of the primer. The fluorescence autocorrelation function of the primer for β-globin gene amplification was identical to that for mtDNA (data not shown). These results suggested that the LPCR product diffused much slower than the primer due to its longer length.

By fitting the autocorrelation function of the primer for mtDNA amplification to a simple one-component model, where $y = 0$ in Eq. (2), the diffusion time was obtained (Table 1). Then the fluorescence correlation functions of the mtDNA and β-globin LPCR products were fitted to

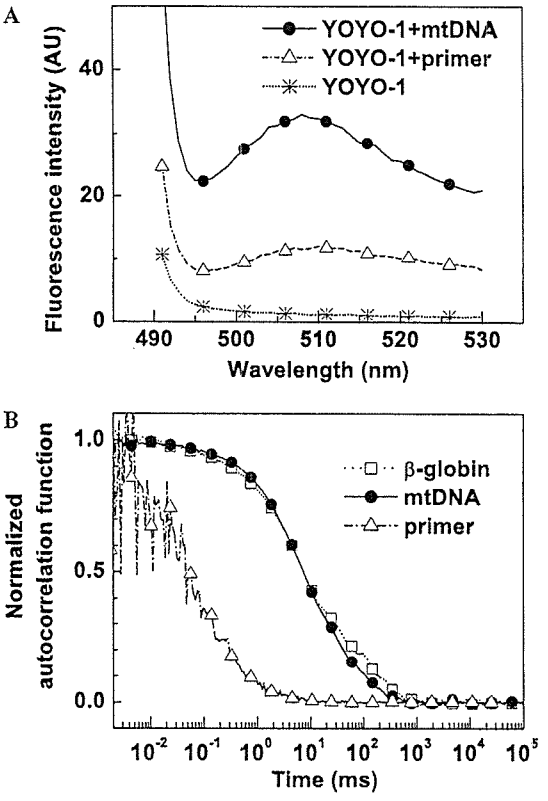

Fig. 1. (A) Fluorescence spectra (●) of 0.5 μM YOYO-1 associated with the mtDNA LPCR product, having an emission maximum at 510 nm. YOYO-1 alone (✳) had little fluorescence at the wavelength. When interacted with the primer for mtDNA amplification, it had a weak fluorescence (Δ), which was one-third the fluorescence in the solution containing the mtDNA LPCR product. (B) Typical normalized autocorrelation functions of the LPCR products of mtDNA and β-globin and the primer for mtDNA amplification.

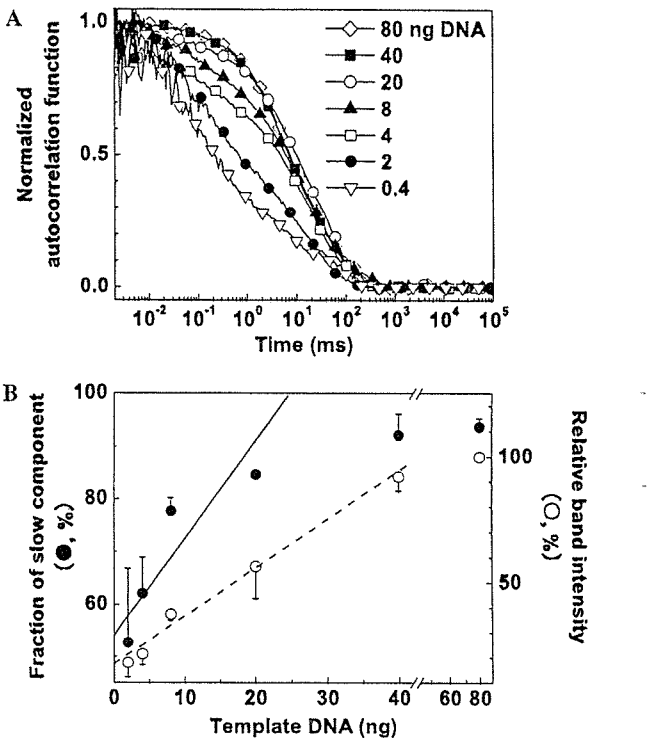

Fig. 2. (A) Changes in normalized autocorrelation functions of mtDNA LPCR products due to the amount of template DNA (0.4–80 ng). (B) Dependence of amount of template DNA on the fraction of the slow component obtained from two-component analysis of the autocorrelation function of the mtDNA LPCR product (●, means + SE) and on relative band intensity by densitometry after gel electrophoresis (○, means − SE). Regression lines are $y = 55 + 1.6x$ ($R = 0.90$) for the fraction of the slow component and $y = 17 + 1.9x$ ($R = 0.99$) for the relative band intensity (2–20 ng of total DNA).

a simple two-component model with a fast-moving component of the free primer and a slow-moving component of the LPCR product using Eq. (2). The diffusion times of the LPCR products ($\tau_{product}$) were determined by curve fitting of autocorrelation data to the two-component model and were found to be 18.2 ± 0.4 ms for mtDNA and 19.6 ± 3.3 ms for β-globin (Table 1). In the following analysis, the obtained values were considered as constant to reduce the number of free parameters.

Dependence of template DNA amount on fraction of slow component

Because the relationship between the amount of template DNA and the number of LPCR products is linear, the fraction was also expected to be dependent on the amount. As shown in Fig. 2A, the autocorrelation function of LPCR products was shifted to the left with the decrease in template DNA from 80 to 0.4 ng, showing a decrease in the slow component. When the functions were analyzed with the two-component model, the fraction of the slow component decreased consistently (Fig. 2B). At more than 20 ng, the fraction seemed to be saturated. The changes in the fraction were similar to the results obtained from densitometry (~17 kbp), although the values of the fraction in FCS were different from those of relative band intensities, which were normalized with the band intensity of 80 ng of template DNA. The results suggest that we can detect the decrease in LPCR product, caused by oxidative stress, if up to 20 ng of template DNA is used under the current conditions of LPCR.

Table 1
Diffusion time of the primer (τ_{primer}) for mtDNA amplification, LPCR products ($\tau_{product}$) for mtDNA, and β-globin

	Primer	mtDNA	β-Globin
Diffusion time (ms)	0.21 ± 0.03	18.2 ± 0.4	19.6 ± 3.3
Number of samples	5	4	3

Note. Values are expressed as means and standard errors.

Effect of H_2O_2 on fraction of slow component

Cells were treated with various concentrations of H_2O_2 up to 1 mM for 1 h. Just after exposure to 1 mM, cells detached from culture dishes. Under conditions up to 0.4 mM, cells remained attached. When cells were treated with 0.4 mM H_2O_2, cell growth was suppressed 2 days after the treatment, probably due to apoptosis [1].

After exposure up to 0.4 mM H_2O_2 for 60 min, total DNA of the cells was extracted. With 20 ng of total DNA as a template, the target sequence was amplified and FCS measurement was conducted. When 0.1 mM H_2O_2 was added, a decrease in the fraction for the mtDNA LPCR product from 79.3 ± 5.4 to $67.9 \pm 3.4\%$ was observed. At 0.4 mM, the fraction was decreased significantly to $53.9 \pm 5.0\%$ (Fig. 3A). The pattern of change was similar to the result of the gel electrophoresis, although the values of fractions obtained by FCS were different from those of relative band intensities, which were normalized with the highest band intensity in each gel. The fraction of the nuclear-encoded β-globin LPCR product remained unchanged, that is, approximately 60% under conditions up to 0.4 mM H_2O_2 (Fig. 3B). H_2O_2-induced mtDNA lesion frequency increased with its dose (Fig. 3C). The frequencies were 0.17 ± 0.07 lesions/10 kb with 0.2 mM treatment and 0.25 ± 0.05 lesions/10 kb with 0.4 mM treatment. We confirmed that there was little effect of H_2O_2 on the β-globin LPCR product on gel. The results shown in Fig. 3 were consistent with those obtained in previous studies indicating that mtDNA was more sensitive than nuclear DNA to H_2O_2 exposure [1,4]. Therefore, the results suggest that oxidative damage of mtDNA can be detected by the LPCR–FCS method.

Primary screening of oxidative stress-induced mtDNA damage

The analysis time of FCS measurement was approximately 5 min, whereas that of gel electrophoresis was more than 3 h, in the current study. The current method is proposed only for a rapid primary screening, not for accurate evaluation of oxidative damage in the mtDNA genome. When the ratio of mtDNA to the nuclear-encoded gene LPCR product is significantly low due to a decrease in the intact mtDNA genome, the screened sample from FCS can be immediately subjected to detailed analysis such as sequencing.

The current measurements of FCS were carried out with a 20-μl sample volume, although theoretically the volume can be reduced to a volume element on the order of 10^{-15} L [9]. Practically, the sample volume for LPCR can be reduced to 1 μl. Thus, this LPCR–FCS method would also have a great advantage from an economic point of view. Physical handling of such a small sample volume can be done by using a capillary tube or a small sample pit on a glass surface covered by a thin film or cover glass for mass examination.

In contrast to common methods used previously without amplification, such as Northern blotting and HPLC–electrochemical detection, target DNA was amplified in our method so that a smaller sample could be employed. Although our method has some of the same limitations as other methods with amplification (e.g., real-time PCR), the DNA sample can be reduced due to the tiny volume element. In this study, we used 20 ng of total DNA. As shown in Fig. 2B, 2 ng of total DNA was sufficient to detect the mtDNA LPCR product. Furthermore, because 30 μg of total DNA was isolated from 10^6 cells, mtDNA damage could be detected using a few hundred cells.

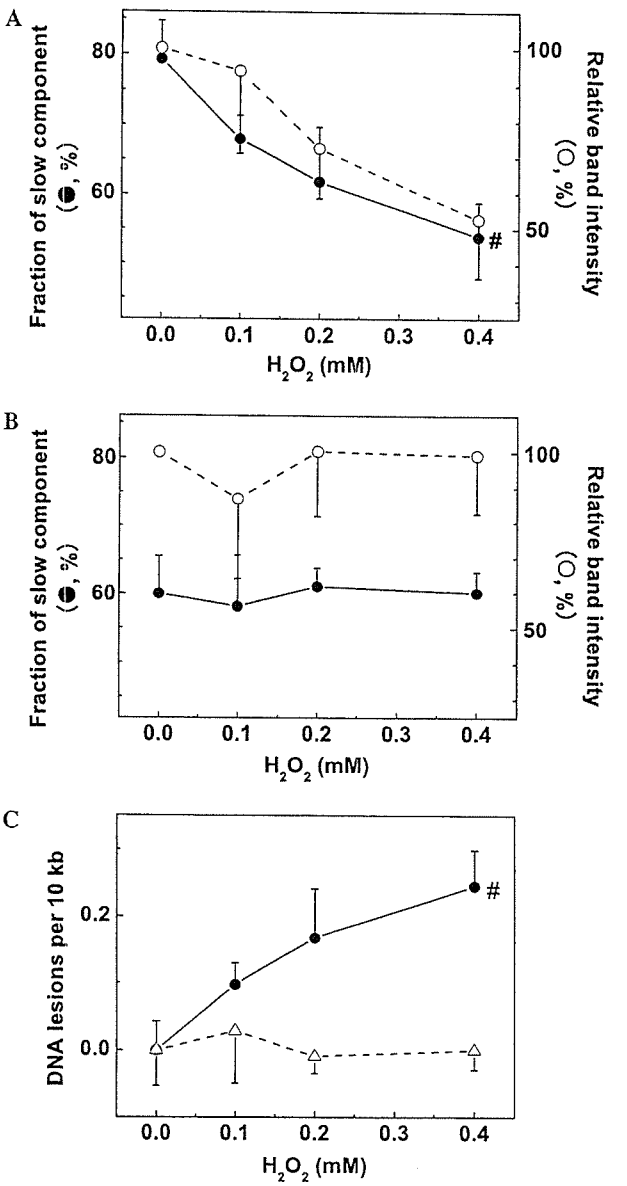

Fig. 3. (A) H_2O_2 dependence on the fraction of the slow component obtained from two-component analysis of the autocorrelation function of the mtDNA LPCR product (●, means + SE) and on relative band intensity obtained by densitometry after gel electrophoresis (○, means − SE). (B) H_2O_2 dependence on the fraction for β-globin. (C) Lesion frequencies in mtDNA (●, means + SE) and β-globin gene (Δ, means − SE), evaluated by FCS. $^{\#}P < 0.05$ compared with the fraction without H_2O_2 treatment.

Currently, real-time PCR may be the most sensitive and precise method for detection and quantification of nucleic acids. However, it is a complex technique and substantial problems are associated with its reproducibility. Furthermore, in contrast to our method measuring after PCR, the real-time PCR method measures fluorescence intensity

during PCR so that its target usually ranges from 100 to 500 bp. If real-time PCR is expanded for a long target sequence, setting the optimal PCR conditions becomes complicated. Our LPCR–FCS method makes possible the evaluation of oxidative stress-induced mtDNA damage without a complex process.

In conclusion, the current method would be advantageous for epidemiological studies to determine the relationship between mtDNA damage and the diseases in which mitochondrial deficiencies might be relevant.

Acknowledgment

This study was supported financially in part by a Grant-in-Aid for Scientific Research (C 2 14580761) from the Ministry of Education, Science, Sports, and Culture of Japan.

References

[1] F.M. Yakes, B. van Houten, Mitochondrial DNA damage is more extensive and persists longer than nuclear DNA damage in human cells following oxidative stress, Proc. Natl. Acad. Sci. USA 94 (1997) 514–519.

[2] W.J. Driggers, S.P. LeDoux, G.L. Wilson, Repair of oxidative damage within the mitochondrial DNA of RINr 38 cells, J. Biol. Chem. 268 (1993) 22042–22045.

[3] J.H. Santos, L. Hunakova, Y. Chen, C. Bortner, B. van Houten, Cell sorting experiments link persistent mitochondrial DNA damage with loss of mitochondrial membrane potential and apoptotic cell death, J. Biol. Chem. 278 (2003) 1728–1734.

[4] G. Wang, T.K. Hazra, S. Mitra, H.M. Lee, E.W. Englander, Mitochondrial DNA damage and a hypoxic response are induced by $CoCl_2$ in rat neuronal PC12 cells, Nucleic Acids Res. 28 (2000) 2135–2140.

[5] M. Deschauer, A. Krasnianski, S. Zierz, R. Taylor, False-positive diagnosis of a single, large-scale mitochondrial DNA deletion by Southern blot analysis: the role of neutral polymorphisms, Genet. Test. 8 (2004) 383–387.

[6] C. Richter, J.W. Park, B.N. Ames, Normal oxidative damage to mitochondrial and nuclear DNA is extensive, Proc. Natl. Acad. Sci. USA 85 (1988) 6465–6467.

[7] S. Cheng, R. Higuchi, M. Stoneking, Complete mitochondrial genome amplification, Nat. Genet. 7 (1994) 350–351.

[8] Y. Nomura, M. Kinjo, Real-time monitoring of in vitro transcriptional RNA using fluorescence correlation spectroscopy, ChemBioChem 5 (2004) 1701–1703.

[9] M. Kinjo, Detection of asymmetric PCR products in homogeneous solution by fluorescence correlation spectroscopy, BioTechniques 25 (1998) 706–715.

[10] M. Kinjo, R. Rigler, Ultrasensitive hybridization analysis using fluorescence correlation spectroscopy, Nucleic Acids Res. 23 (1995) 1795–1799.

[11] Y. Nomura, H. Tanaka, L. Poellinger, F. Higashino, M. Kinjo, Monitoring of in vitro and in vivo translation of green fluorescent protein and its fusion proteins by fluorescence correlation spectroscopy, Cytometry 44 (2001) 1–6.

[12] M. Kinjo, Quantitative analysis by the polymerase chain reaction using fluorescence correlation spectroscopy, Anal. Chim. Acta 365 (1998) 43–48.

[13] R. Rigler, U. Mets, J. Widengren, P. Kask, Fluorescence correlation spectroscopy with high count rate and low background: analysis of translational diffusion, Eur. Biophys. J. 22 (1993) 166–175.

[14] S. Aragon, R. Pecora, Fluorescence correlation spectroscopy as a probe of molecular dynamics, J. Chem. Phys. 64 (1976) 1791–1803.

[15] D.P. Kalinowski, S. Illenye, B. Van Houten, Analysis of DNA damage and repair in murine leukemia L1210 cells using a quantitative polymerase chain reaction assay, Nucleic Acids Res. 20 (1992) 3485–3494.

Expert Opinion

Gene Therapy

Gene therapy for Parkinson's disease using recombinant adeno-associated viral vectors

Shin-ichi Muramatsu†, Hideo Tsukada, Imaharu Nakano & Keiya Ozawa
†Jichi Medical School, Division of Neurology, Department of Medicine, 3311-1 Yakushiji, Minami-kawachi, Tochigi, 3290498 Japan

Existing strategies for gene therapy in the treatment of Parkinson's disease include the delivery of genes encoding dopamine (DA)-synthesising enzymes, leading to localised production of DA in the striatum; genes encoding factors that protect nigral neurons against ongoing degeneration, such as glial cell line-derived neurotrophic factor; and genes encoding proteins that produce the inhibitory transmitter γ-aminobutylic acid (GABA) in the subthalamic nucleus (STN), thus suppressing the hyperactive STN. Recombinant adeno-associated viral (rAAV) vectors, which are derived from non-pathogenic viruses, have been shown to be suitable for clinical trials. These rAAVs have been found to transduce substantial numbers of neurons efficiently and to express transgenes in mammalian brains for long periods of time, with minimum inflammatory and immunological responses. *In vivo* imaging using positron emission tomography is useful for monitoring transgene expression and for assessing the functional effects of gene delivery. Vector systems that regulate transgene expression are necessary to increase safety in clinical applications, and the development of such systems is in progress.

Keywords: AAV, adeno-associated virus, dopamine, gene therapy, glial cell line-derived neurotrophic factor, Parkinson's disease, positron emission tomography

Expert Opin. Biol. Ther. (2005) 5(5):663-671

1. Introduction

Parkinson's disease (PD) is a common neurodegenerative disorder among the elderly, with an estimated prevalence of 1% in individuals > 60 years old. During the progression of PD there is a loss of neurons in the substantia nigra pars compacta (SNc), which projects to the striatum (caudate and putamen), leading to a substantial decrease in the dopamine (DA) content of the striatum. Although our understanding of the molecular basis of PD has advanced following the identification of mutations in the *α-synuclein*, *parkin*, *DJ-1*, *PINK1* and *LRRK2* genes associated with familial PD [1-3], the cause of PD largely remains unknown and to date there is no curative therapy.

The primary symptoms of PD are motor disturbances, including resting tremor, muscular rigidity and bradykinesia. These symptoms become apparent after 40 – 50% of the neurons in the SNc have been lost and striatal DA has been reduced to ~ 20% of normal levels [4]. The introduction of the DA precursor L-3,4-dihydroxyphenylalanine (L-dopa) in the late 1960s represented a major therapeutic advance in the management of PD, demonstrating that the replacement of DA is important in alleviating the motor symptoms of this disease. Although virtually all PD patients benefit clinically from L-dopa therapy, L-dopa becomes less effective as the disease progresses. Frequent systemic administration of high-dose L-dopa causes oscillations in motor performance [5,6] and deleterious

complications, including hallucinations due to dopaminergic stimulation of the mesolimbic system [7]. Thus, novel therapeutic interventions that complement or substitute for oral L-dopa administration are required.

Unlike other neurological disorders that affect broad regions of the brain, PD is primarily confined to the well-defined nigrostriatal dopaminergic system. Stereotactic techniques based on microelectrode recording of neural activities and magnetic resonance imaging-assisted navigation have become established in clinical practice and can be used in gene therapy to deliver vectors into the striatum.

2. Recombinant adeno-associated viral vectors

Among the various gene delivery vehicles tested preclinically for PD, the recombinant adeno-associated viral (rAAV) vector has been found most suitable for clinical applications, due to both its efficacy and safety. This vector is the only one based on the use of a non-pathogenic and replication-defective virus. Efficient and long-term gene expression has been achieved in mammalian brains without substantial toxicity or immune response [8-11]. Wild-type adeno-associated viruses (AAVs) are small, non-enveloped, single-stranded DNA viruses of the *Parvoviridae* family assigned to the genus *Dependovirus*. Productive infection with AAV has been found to require coinfection with a helper virus, such as adenovirus or herpes virus [12]. Until the mid-1990s, only AAV serotype 2 (AAV-2) had been sequenced, making it a major platform for gene therapy vector development [13-20]. So far > 100 different AAV sequences have been isolated from human and non-human primates [21], and their recombinants have been investigated extensively for tissue tropism and transduction efficiency. This has led to an increase in transduction efficiency, as well as being associated with changes in tissue or cell type tropism or vector distribution patterns in a given tissue [22-26].

Although chromosomal rearrangements in association with rAAV integration have been observed in a transformed cell line [27] and in regenerating hepatocytes [28], rAAV is more commonly present *in vivo* as duplex, circular and head-to-tail concatemers, most of which are episomal in non-dividing cells in the absence of selection [29]. Preferential integration into active regions of the chromosome and into actively transcribed genes is not unique to rAAV vectors [30], inasmuch as it has been noted even in adenoviruses, which are generally considered to be non-integrating. In addition, the promoter activity of the terminal repeat sequence of AAV is much weaker than that of retrovirus, probably limiting transcription to the inward direction of the viral genome. Thus, the risks of insertional mutagenesis and activation of oncogenes are quite low. Other safety aspects of rAAV vectors have been reviewed elsewhere [31,32].

Pre-existing antibodies to naturally infecting AAV-2 are found in 80% of the human population, and neutralising antibodies can be induced after rAAV vector administration. These antibodies may compromise transgene expression [33,34], and the presence of elevated neutralising antibody titres should be considered as exclusion criteria for clinical trials, although further studies are necessary to more specifically define the antibody titre that would constitute exclusion. Different rAAV vector serotypes will permit successful retransduction in response to significant levels of neutralising antibodies to one or more rAAV vectors.

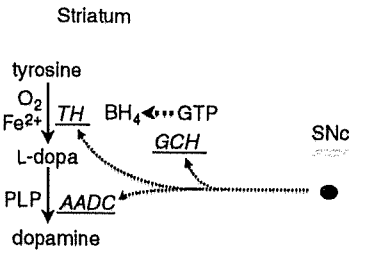

Figure 1. Biosynthetic pathway of DA. Three enzymes are necessary for efficient DA production. TH converts dietary tyrosine into L-dopa, which in turn is converted into DA by AADC. GCH is the rate-limiting enzyme for the biosynthesis of BH_4, the essential TH cofactor. All three of these enzymes are synthesised in the substantia nigra and transported to the striatum. Drastic reduction in the activities of these enzymes results in the depletion of DA in the striatum, leading to the manifestation of motor symptoms.
AADC: Aromatic-L-amino acid decarboxylase; BH_4: Tetrahydrobiopterin; DA: Dopamine; GCH: Guanosine triphosphate cyclohydrolase I; GTP: Guanosine triphosphate; L-dopa: L-3,4-dihydroxyphenylalanine; PLP: Pyridoxal 5'-phosphate; SNc: Substantia nigra pars compacta; TH: Tyrosine hydroxylase.

3. Local production of dopamine in the striatum

3.1 Biosynthesis of dopamine

One potential strategy of gene therapy for PD is to restore local production of DA by delivering genes of DA-synthesising enzymes into the striatum [9-11,35-39]. Three enzymes are necessary for efficient DA synthesis: tyrosine hydroxylase (TH), aromatic L-amino acid decarboxylase (AADC) and guanosine triphosphate cyclohydrolase I (GCH) (Figure 1). TH is the rate-limiting enzyme that converts L-tyrosine to L-dopa; AADC converts L-dopa to DA; and GCH is the rate-limiting enzyme in the biosynthesis of the essential TH cofactor, tetrahydrobiopterine (BH_4). These three enzymes are synthesised in SNc neurons and are anterogradely transported to the striatum. In advanced PD, the severe loss of dopaminergic nerve terminals is associated with an 80 – 95% depletion of striatal TH and AADC activity [40-42], leading to a profound decrease in DA. Failure to respond to L-dopa therapy may result from a reduction in AADC activity, decreased DA storage capacity in synaptic vesicles, postsynaptic changes in striatal output neurons and/or abnormalities of non-dopaminergic neurotransmitter systems. AADC is present in DA-denervated striatum within non-dopaminergic neurons and glial cells, but endogenous AADC activity in the